J. Fluid Mech. (2016), *vol.* 802, *pp.* 775–805.
doi:10.1017/jfm.2016.468

Droplet impact on a thin liquid film: anatomy of the splash

Christophe Josserand[1,2,†], Pascal Ray[1,2] and Stéphane Zaleski[1,2]

[1]Sorbonne Universités, UPMC Univ Paris 06, UMR 7190, Institut Jean Le Rond d'Alembert, F-75005, Paris, France

[2]CNRS, UMR 7190, Institut Jean Le Rond d'Alembert, F-75005, Paris, France

(Received 30 November 2015; revised 6 May 2016; accepted 12 July 2016)

We investigate the dynamics of drop impact on a thin liquid film at short times in order to identify the mechanisms of splash formation. Using numerical simulations and scaling analysis, we show that it depends both on the inertial dynamics of the liquid and the cushioning of the gas. Two asymptotic regimes are identified, characterized by a new dimensionless number J: when the gas cushioning is weak, the jet is formed after a sequence of bubbles are entrapped and the jet speed is mostly selected by the Reynolds number of the impact. On the other hand, when the air cushioning is important, the lubrication of the gas beneath the drop and the liquid film controls the dynamics, leading to a single bubble entrapment and a weaker jet velocity.

Key words: drops, drops and bubbles, interfacial flows (free surface)

1. Introduction

Droplet collisions and impacts are iconic multiphase flow problems: rain, atomization of liquid jets, ink-jet printing and stalagmite growth all involve impact in one manner or another (Rein 1993; Yarin 2006; Josserand & Thoroddsen 2016). The droplet may impact on a dry surface, a thin liquid film or a deep liquid bath. In all cases, impact may lead to the spreading of the droplet or to a splash whereby a myriad of smaller droplets are ejected far away from the zone of impact (Rioboo, Marengo & Tropea 2001). Control of the outcome of impact is crucial for applications: for instance, spreading is desirable for coating or ink-jet printing while splashing may improve the efficiency of evaporation and mixing in combustion chambers. Two distinct types of splash, 'prompt' and 'ordinary', are now usually distinguished. The prompt splash is defined as a very early ejection of liquid at a time $t \ll D/U_0$ where D is the droplet diameter and U_0 its velocity. A very thin liquid jet is formed, called the ejecta sheet (Thoroddsen 2002), projected at high velocity, initially almost horizontally, and it is expected to disintegrate eventually into very small and rapid droplets. The second type of splash, often called also the corolla or crown splash, occurs at later times, through the formation of a vertical corolla ending in a circular rim that destabilizes into fingers and droplets (Deegan, Brunet & Eggers 2008; Agbaglah *et al.* 2015).

† Email address for correspondence: christophe.josserand@upmc.fr

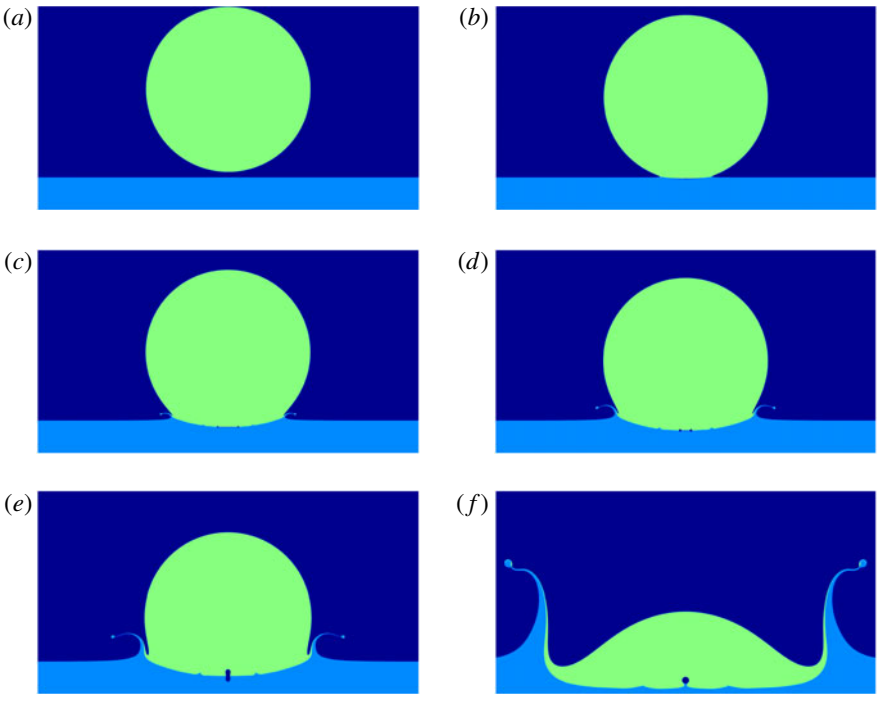

FIGURE 1. (Colour online) Snapshots of a droplet impacting on a thin liquid film for the parameters in tables 1 and 2, i.e. $We = 500$, $Re = 2000$ and $St = 2.26 \times 10^{-6}$, so that the jet number is $J = 0.041$. For the sake of visualization, the liquid of the droplet and of the layer have been coloured green and blue respectively, although it is the same liquid. The gas phase is coloured dark blue. The snapshots correspond to the dimensionless times $U_0 t/D = -0.033$, 0.0167, 0.083, 0.133, 0.217 and 0.767 respectively.

Very often, these two mechanisms are not easy to distinguish clearly since they happen in a sequence, the ejecta sheet being a precursor of the corolla, as illustrated by the numerical simulations of a droplet impact on a thin liquid film, shown in figure 1.

The dynamics of droplet impact is complex, involving singular surface deformation and pressure values in the inviscid limit and several instabilities of surface evolution, so that an overall understanding of the whole process is still lacking. In particular, the splash depends on many physical parameters, the most important being the impact velocity. Obviously, high velocities promote the splash while at low velocities the droplet gently spreads. More precisely, the splashing–spreading transition depends mostly on the balance, in the liquid, between inertial and viscous forces (Stow & Hadfield 1981; Mundo, Sommerfeld & Tropea 1995; Yarin & Weiss 1995; Josserand & Zaleski 2003), characterized by the Reynolds and Weber numbers defined below. Although droplet impact on a solid surface or on a liquid film shows similar outputs, the physical mechanisms leading to these effects often have different origins. For droplet impact on solids, the surface properties play an important role, through its roughness and the contact line dynamics for instance. There, a remarkable discovery has been made recently: the surrounding gas (usually air) also plays a crucial role in splash formation (Xu, Zhang & Nagel 2005), and understanding in detail the influence

of the gas remains a challenge (Mandre & Brenner 2012; Klaseboer, Manica & Chan 2014; Riboux & Gordillo 2014). In particular, the formation of a thin air layer at the instant of impact smooths the singularity expected in the absence of any gas and thus 'cushions' the impact, leading to the entrapment of an air bubble (Mehdi-Nejad, Mostaghimi & Chandra 2003; Thoroddsen, Etoh & Takehara 2003; Thoroddsen *et al.* 2005; Mandre, Mani & Brenner 2009; Duchemin & Josserand 2011). For drop impact on a liquid, the thickness of the liquid film is crucial and the corolla splash can be seen as the result of the collision between the spreading drop and the liquid layer at rest (Yarin & Weiss 1995). There also, as has been noted experimentally and numerically, air bubbles are entrapped by the impact dynamics (Thoroddsen *et al.* 2003; Thoraval *et al.* 2012), although the effect of the surrounding air has been shown not to be as dramatic as on solid surfaces. However, a systematic study of its influence on the impact outputs is still lacking and a potential interplay between the bubble entrapment and the ejecta sheet still needs to be elucidated. In 2003, two of us (Josserand & Zaleski 2003, which we hereafter refer to as JZ03) proposed that the splashing–spreading transition observed in experiments and in numerics was controlled by the capillary–inertia balance within the ejecta sheet. The thickness in this theory was selected by a viscous boundary layer. In such a model, scaling laws for the jet thickness and velocity were deduced, neglecting the gas dynamics, and the existence of an entrapped bubble was not considered.

The goal of this paper is therefore to determine the properties of the ejecta sheet for the splashing of a drop on a thin liquid film, with a particular emphasis on the interaction between the jet formation and the gas dynamics. High-resolution numerical simulations of axisymmetric incompressible Newtonian two-phase flow will be used in order to exhibit the relevant physical mechanisms at the heart of the prompt splash in this framework.

2. The general problem

2.1. *Geometry and dimensional analysis*

We consider a droplet of diameter D impacting on a thin liquid film of thickness e with a velocity U_0 normal to the film interface. The liquid and gas have densities ρ_l and ρ_g and dynamical viscosities μ_l and μ_g respectively. The surface tension is σ. In experiments the droplet impact is typically produced by the release of a drop at some height H above the film, falling under gravity g. In our case, the simulation starts with a small initial air gap h_0 between the film and the droplet and a velocity U_0, as shown in figure 2. The droplet is assumed to be spherical. In order for this assumption to be valid we need (i) to have as little effect of the air flow on the droplet shape as possible, which should be verified if the gas Weber number $We_g = \rho_g U_0^2 D/\sigma$ is small or in a viscous regime, and (ii) to assume that the oscillations of the droplet shape caused by the droplet release mechanism (Wang, Kuan & Tsai 2013) are as small as possible. The Froude number $Fr = U_0^2/(gD)$ that quantifies the influence of gravity during the impact is taken as constant and high ($Fr = 800$) for all the simulations, indicating that gravity has only a small effect on the dynamics. We will restrict this study to large liquid Weber numbers $We = \rho_l U_0^2 D/\sigma$.

The problem is then mostly characterized by the dimensionless numbers

$$Re = \frac{\rho_l U_0 D}{\mu_l}, \quad St = \frac{\mu_g}{\rho_l U_0 D} \quad \text{and} \quad \alpha = \frac{\rho_g}{\rho_l}, \tag{2.1a–c}$$

which are the liquid Reynolds and Stokes numbers of the impact and the density ratio. These numbers compare the droplet inertia with viscous effects in the liquid

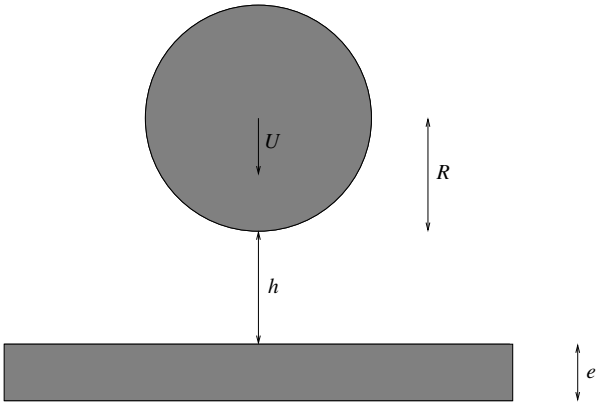

FIGURE 2. Sketch of the numerical simulation. A spherical droplet of radius R and velocity U_0 is considered at a distance h_0 from a liquid film of thickness e.

and gas, respectively, and compare the liquid to the gas inertia. We note that ρ_l/ρ_g has to be very large if one wants simultaneously to have $We_g \ll 1$ and $We \gg 1$. An additional dimensionless number is the aspect ratio between the liquid film and the droplet, e/D, which we keep relatively small and constant in this study. We expect the initial gas layer aspect ratio h_0/D to be irrelevant if the conditions described above ($Fr \gg 1$, $We_g < 1$) are satisfied and h_0 is larger than the characteristic thickness h_b defined below. Compressibility effects are characterized by the Mach numbers $Ma = U/a_{l,g}$, where a_l (respectively a_g) is the speed of sound in the liquid (respectively gas), and in all our simulations these Mach numbers remain small enough so that compressibility effects can be neglected (Lesser & Field 1983).

We note that the axisymmetric flow assumption is not valid when digitations and splash droplets form. However, at short times, before these instabilities can develop and particularly before the jet is created, we can consider this assumption correct (Agbaglah & Deegan 2014). Otherwise the general three-dimensional (3-D) problem remains a grand numerical challenge because of the large range of scales involved (Gueyffier & Zaleski 1998; Rieber & Frohn 1998). Despite some recent numerical results (Fuster *et al.* 2009), realistic 3-D numerical simulations of droplet impact at short times are as yet hard to attain. Moreover, a solid basis for the analysis of the scaling of 3-D flow may only be attained when the scaling of 2-D flow has been uncovered. We thus postpone a detailed 3-D study of droplet impact for future work.

2.2. *Scaling analysis*

We analyse now the different mechanisms at play during droplet impact using simple scaling arguments. Recall that surface tension and gravity can be neglected, and in a first step, we will consider also that the surrounding gas has negligible effects. We then quite naturally define $t = 0$ as the time at which the undeformed, spherical droplet at uniform velocity would touch the undeformed, planar liquid surface. With this definition of time, the initial time is $t_0 = -h_0/U_0$.

We will now use an important geometrical argument first suggested by Wagner (1932): considering the intersection of the falling sphere with the impacted film, it is straightforward to define the vertical length scale as $\ell_z = U_0 t$ and the horizontal

one as $r_g = \sqrt{D\ell_z} = \sqrt{DU_0 t}$. These apparently simple scalings arising purely from geometry are in fact very robust and relevant to the description of impact at short times: for instance, it has been shown that $r_g(t)$ gives a correct estimate of the so-called spreading radius, defined as the radius where the pressure is maximal (JZ03). Remarkably, the geometrical velocity of this intersection,

$$v_g(t) = \frac{\mathrm{d}r_g}{\mathrm{d}t} = \frac{1}{2}\sqrt{\frac{DU_0}{t}}, \tag{2.2}$$

diverges at $t = 0$, questioning the incompressible assumption. However, although formally such a geometrical velocity diverges, fluid velocities remain much smaller and compressibility can be safely neglected for small Mach numbers. To make the article self-contained, we will now recall briefly the results obtained by JZ03. The key point is the numerical observation that the pressure field and the velocity field are perturbed over the length scale $r_g(t)$ so that a kind of inner–outer asymptotic analysis can be performed, in which the flow is uniform at scales larger than r_g, potential at scales of order r_g and viscous at scales much smaller than r_g (a more rigorous asymptotic analysis was developed later in Howison *et al.* (2005)). In this analysis the ejecta speed is obtained using a mass conservation argument between the impacting droplet and the ejected sheet, assuming that the thickness of the jet is selected by a viscous length. More precisely, one can compute in this framework first the mass flux F_m from the falling undeformed sphere through the undeformed film surface,

$$F_m(t) \sim \rho_l \pi r_g^2 U_0. \tag{2.3}$$

This flux can be absorbed either by surface deformation of the droplet and of the film or by the formation of an ejecta sheet. In JZ03, we have assumed that the thickness of such a sheet or jet is given by a viscous boundary layer formed at the base of the jet, leading to a viscous length scale

$$e_j(t) \sim \sqrt{\frac{\mu_l t}{\rho_l}}. \tag{2.4}$$

Then, conservation of the volume flux through this jet implies that the jet velocity U_j has to satisfy

$$U_j \sim \sqrt{Re}\, U_0. \tag{2.5}$$

Remarkably, this gives a nonlinear relationship between the jet and the impacting droplet velocity since then $U_j \propto U_0^{3/2}$. Such a law has obviously some physical restrictions: first of all, the flux formula (2.3) is valid only for $t \ll R/(2U_0)$ since our whole analysis is for short times and makes no sense for times of order D/U_0. Furthermore, the jet velocity has to be larger than the geometrical velocity v_g. Indeed, if $U_j < v_g(t)$ one would expect the ejecta sheet to be overrun by the falling droplet. This condition together with (2.2) yields a 'geometric' limiting time t_g:

$$t > t_g \sim \frac{1}{Re}\frac{D}{U_0}. \tag{2.6}$$

When the ejecta forms, a bulge or rim appears at its tip according to the mechanism of Taylor (1959) and Culick (1960). This rim moves backwards at the Taylor–Culick velocity

$$v_{TC} = \sqrt{\frac{2\sigma}{\rho_l e_j}}, \tag{2.7}$$

where e_j is the thickness of the ejecta sheet. The ejecta sheet cannot form if its velocity is smaller than the Taylor–Culick velocity constructed with the thickness e_j of the ejecta sheet. We thus obtain that the ejecta can form only when $U_j > v_{TC}$, which from equations (2.5), (2.4) and (2.7) yields

$$t > t_{TC} = \frac{2}{We^2\, Re}\frac{D}{U_0}. \tag{2.8}$$

Both conditions (2.6) and (2.8) must be satisfied at short times $t \ll D/U_0$ because, as stated above, the whole theory does not make sense for larger times. Then we must have $\max(t_{TC}, t_g) \ll D/U_0$, which yields the condition

$$\min(We^2\, Re, Re) \gg 1. \tag{2.9}$$

Since we restrict the present study to the dynamics where splashing is always present, we consider situations such that $We \gg 1$ and $Re \gg 1$, so that of the two conditions for splashing given above, $t > t_g$ is always more restrictive than $t > t_{TC}$. Therefore, in our configuration, the jet appears only when its velocity is bigger than the geometrical one. Interestingly, this analysis suggests that for $t < t_g$, jets can form but are immediately absorbed by the geometrical advancement of the drop on the liquid layer.

Finally, the inertial pressure of the impact, P_{imp}, can be computed using the rate of change of vertical momentum in the droplet, following JZ03:

$$P_{imp}\pi r_g^2 \sim \frac{2\pi}{3}\rho_l r_g^3 U_0 \frac{\mathrm{d}r_g}{\mathrm{d}t}. \tag{2.10}$$

In this equation, the vertical momentum in the droplet is affected only in a half-sphere of radius r_g. Equation (2.10) gives the impact pressure

$$P_{imp} \sim 2\rho_l \frac{\mathrm{d}r_b}{\mathrm{d}t} U_0, \tag{2.11}$$

which leads to

$$P_{imp} \sim \sqrt{\frac{D}{U_0 t}}\rho_l U_0^2 \tag{2.12}$$

as observed in numerical simulations (see JZ03). Note that a detailed analysis of the potential flow for a droplet falling onto a solid surface has been performed by Philippi, Lagrée & Antkowiak (2016). The reasoning in the latter paper may be straightforwardly transposed to the impact on a liquid surface to obtain for the pressure field in the neighbourhood of $z = 0$

$$p(r, t) \sim \frac{3\rho_l U_0^2}{\pi\sqrt{\dfrac{3tU_0}{R} - \dfrac{r^2}{R^2}}}, \tag{2.13}$$

which is very similar at $r = 0$ to the scaling in (2.12). However, the pressure field of (2.13) has an additional singularity for $t > 0$ not predicted by (2.12) at $r = \pm\sqrt{3RU_0 t}$. This singularity is indeed observed in our numerical simulations as well as in JZ03, Duchemin & Josserand (2011) and Philippi *et al.* (2016).

In the theory above, contact occurs at $t=0$, the vertical length scales are $U_0 t$ and e_j, and the flow pressure and the geometric velocity are singular with an infinite limit at $t=0$. So far, the effect of the gas layer has not been considered. When instead the gas layer is taken into account, the above analysis is an approximation valid at length scales $\ell \gg h_b$ where h_b is the thickness of the gas layer involved in the cushioning due to its viscosity. The scale of the impact pressure is thus, following equation (2.12),

$$P_{imp} \sim \sqrt{\frac{D}{h_b}} \rho_l U_0^2. \tag{2.14}$$

The singularity of the velocity and the pressure is thus regularized by the gas viscosity so that it can be said that the gas 'cushions' the shock of the impact.

Furthermore, it is observed in experiments by Thoroddsen *et al.* (2003) and in numerical simulations (Josserand & Zaleski 2003; Mehdi-Nejad *et al.* 2003; Korobkin, Ellis & Smith 2008) that contact does not occur on the symmetry axis $r=0$ but on a circle of radius r_b so that a bubble is entrapped, as observed also for droplet impact on solid surfaces by Thoroddsen *et al.* (2005) and Kolinski *et al.* (2012). As before, horizontal and vertical length scales are related at short times by $l_z \sim l_r^2/D$, so that we have the thickness h_b of the gas layer or entrapped bubble at the time of contact related to the contact radius r_b by

$$h_b = r_b^2/D. \tag{2.15}$$

These short-time asymptotics have to match the initial conditions at negative time $t=-t_0$. Let $z_+(r,\,t)$ and $z_-(r,\,t)$ be the positions of the drop and film surfaces, respectively, and let $h(r,\,t)=z_+(r,\,t)-z_-(r,\,t)$ be the thickness of the gas layer. To fix ideas, let us consider initial conditions such that $z_-(r,\,-t_0)=0$ and $h(r,\,-t_0)=z_+(r,\,-t_0)$ close to the impact time so that on the axis $h(0,\,-t_0)=h_0 \ll D$. The gas layer is therefore thin and there is a separation of horizontal and vertical length scales so that the lubrication approximation is valid over distances $l_r \sim \sqrt{h(0,\,-t)D}$. As long as the lubrication pressure (estimated below) thus obtained in the gas layer is much smaller than the impact pressure P_{imp}, the liquid advances almost undeformed while expelling the gas. In this regime

$$\partial_t h(0,\,t) = -U_0. \tag{2.16}$$

When the lubrication pressure becomes large enough to deform the liquid and slow down the thinning of the gas layer, the time is of the order of the so-called air-cushioning time scale t_b and the thickness reaches the air-cushioning length scale h_b. Matching with the initial velocity, equation (2.16) then gives the relationship $h_b = U_0 t_b$, which together with the separation of scales condition (2.15) links the time and position of the contact through $t_b \sim r_b^2/(DU_0)$.

In order to determine these air-cushioning space and time scales, we find the dominant balance in the lubrication equation, following in part recent works on impacts onto solid surfaces (Korobkin *et al.* 2008; Mandre *et al.* 2009; Hicks & Purvis 2010; Duchemin & Josserand 2011; Hicks & Purvis 2011, 2013; Klaseboer *et al.* 2014). Our theory starts from the incompressible lubrication equation in a cylindrical geometry:

$$\partial_t h = \frac{1}{12\mu_g r} \partial_r (r h^3 \partial_r P), \tag{2.17}$$

where $P(r,\ t)$ is the pressure in the gas layer. The factor $1/12$ in front of the lubrication pressure comes from the Poiseuille velocity profile valid for laminar flows, obtained with a zero radial velocity at z_- and z_+, which is assumed because of the small horizontal velocity in the liquid before splashing. Using the above geometrical argument, $h \sim \sqrt{Dr}$ for the pressure term and $\partial_t h \sim -U_0$, we obtain the following scaling for the lubrication pressure P_b in the gas film of thickness h:

$$P_b \sim \frac{3\mu_g U_0 D}{h^2}, \tag{2.18}$$

The usual lubrication scaling for the bubble entrapment is then obtained by writing that during this 'cushioning phase', the air pressure for $h \sim h_b$ balances the impact pressure, i.e. $P_b \sim P_{imp}$, yielding

$$P_b \sim \frac{3\mu_g U_0 D}{h_b^2} \sim P_{imp} \sim \rho_l U_0^2 \sqrt{\frac{D}{U_0 t_b}} \sim \rho_l U_0^2 \sqrt{\frac{D}{h_b}}, \tag{2.19}$$

using the relation $h_b = U_0 t_b$ deduced above. This relation gives the following scalings for the bubble entrapment:

$$h_b \sim St^{2/3}\, D, \quad r_b \sim St^{1/3}\, D, \quad t_b \sim \frac{h_b}{U_0} \sim St^{2/3} \frac{D}{U_0} \quad \text{and} \quad P_b \sim \frac{3\mu_g U_0 D}{h_b^2} \sim 3\rho_l U_0^2\, St^{-1/3}. \tag{2.20a–d}$$

The cushioning phase starts when t is negative and of order $-t_b$ and ends when first contact occurs at a positive time t_b. This leads to two remarks: one is that the time of 'cushioning' t_b is both the time scale of the duration of this phase and the time coordinate of the two instants at the beginning of the cushioning phase and at the end of it when first contact occurs. We do not have strong arguments or data to show that these two instants are symmetric around $t = 0$. However, interestingly, our numerical simulations show that a kind of droplet/film symmetry holds, so that at $t = 0$, we have to a high degree of accuracy $z_+(0,\ 0) = -z_-(0,\ 0)$ (see figure 4 below).

In this approach, in agreement with previous works (Mandre *et al.* 2009; Duchemin & Josserand 2011), gas inertia effects have been neglected, although such an assumption is questionable, as suggested in a recent work on impacts onto solid surfaces (Mani, Mandre & Brenner 2010; Riboux & Gordillo 2014). Implementing the corrections due to inertial effects in the thin film equation remains a difficult problem to tackle analytically (Wilson & Duffy 1998; Luchini & Charru 2010) so we provide here only estimates based on scaling analysis.

The variation of the film height is given by the divergence of the horizontal gas flux in the layer:

$$\partial_t h = -\frac{1}{r}\partial_r(rh\bar{u}), \tag{2.21}$$

where $\bar{u}$ is the averaged horizontal velocity between z_- and z_+. We can determine the scale u_b for $\bar{u}(r,\ t)$ by considering the momentum balance in a thin gas layer:

$$\partial_t \bar{u} + A\bar{u}\partial_r \bar{u} = -\frac{1}{\rho_g}\,\partial_r p - 12\mu_g \bar{u}/h^2 - K\bar{u}^2/h, \tag{2.22}$$

where A is a constant depending on the profile of the flow in the gas layer and K is a constant characterizing turbulent friction. This equation will hold if the flow

remains thin ($h \ll D$) and does not separate. Since in incompressible flow the pressure is defined up to a constant and the pressure at the exit of the thin gas layer flow (taken here for $r \sim r_g(t)$) is the pressure at infinity, it is convenient to set this pressure at the exit to zero. Then P_b equals the pressure difference and it can be estimated at the bubble entrapment, yielding

$$P_b = 12\mu_g r_b u_b/h_b^2 + C_1\rho_g u_b^2 r_b/h_b + C_2\rho_g u_b^2. \tag{2.23}$$

Here, we have taken for the first (dominant) term the lubrication pressure already computed above. The second and third terms result from two kinds of inertial effects, the turbulent friction term and a possible singular head loss due to flow separation. It is readily seen that the ratio between the first two terms is the local Reynolds number of the gas layer, $\rho_g u_b h_b/\mu_g$. The third term is a singular head loss. The constants C_1 and C_2 depend on the precise geometry of the flow and are difficult to estimate. However, it can be seen that the singular head loss is much smaller for our problem, by a factor of $h/r_g = (DU_0/t_b)^{-1/2}$, than the turbulent friction term so that we will neglect the singular head loss in the following developments.

The film pressure may be finally obtained by estimating the horizontal velocity scale as $u_b = r_b/t_b$, which together with (2.15) yields

$$P_b \sim \frac{12\mu_g U_0 D}{h_b^2} + C_1\rho_g U_0^2\left(\frac{D}{h_b}\right)^{3/2}. \tag{2.24}$$

Remarkably, the neglected singular head loss term would give an additional contribution in the form $C_2\rho_g U_0^2 D/h_b$.

Finally, equating P_b and P_{imp} yields now an implicit equation for h_b:

$$\rho_l U_0^2\left(\frac{D}{h_b}\right)^{1/2} = \frac{12\mu_g U_0 D}{h_b^2} + C_1\rho_g U_0^2\left(\frac{D}{h_b}\right)^{3/2}, \tag{2.25}$$

which can be written in terms of the dimensionless variables $\hat{h}_b = h_b/D$, St and α as

$$12\,St = \hat{h}_b^{3/2} - C_1\alpha\hat{h}_b^{1/2}. \tag{2.26}$$

The above equation is cubic in $\xi = \hat{h}_b^{1/2}$ and its solution gives the dimensionless height of the film as a function of St and α, with two asymptotic regimes separated by a critical Stokes number

$$St_c = \tfrac{1}{12}(C_1\alpha)^{3/2}. \tag{2.27}$$

The first regime, for $St \gg St_c$, corresponds to the case computed above with lubrication only, (2.20), and is of the form

$$\hat{h}_b \sim St^{2/3}, \tag{2.28}$$

as also stated by Mandre *et al.* (2009) and Mani *et al.* (2010). In the other regime, for $St \ll St_c$, we obtain

$$\hat{h}_b \sim C_1\alpha. \tag{2.29}$$

The estimates for the time at which the bubble is entrapped result from the estimates for h_b through $t_b = h_b/U_0$. For $St \gg St_c$ we recover (2.20):

$$\hat{t}_b \sim St^{2/3}, \tag{2.30}$$

where the dimensionless time is $\hat{t} = U_0 t/D$ and all the other scalings are obtained straightforwardly from the scalings for the height $\hat{h}_b$ given above. In particular, the time scale of bubble entrapment $\hat{t}_b$ can be deduced from that of $\hat{h}_b$, taking into account the inertial correction equation (2.26), yielding the same relation (since $\hat{h}_b = \hat{t}_b$):

$$12\,St = \hat{t}_b^{3/2} - C_1 \alpha \hat{t}_b^{1/2}. \tag{2.31}$$

Similarly, from equation (2.12) the pressure in and on top of the gas layer, neglecting surface tension effects, is (2.20):

$$P_{imp,max} \sim \rho_l U_0^2\, St^{-1/3}. \tag{2.32}$$

This theory will now serve as a framework for interpreting the numerical simulations reported below. The main prediction is that air delays contact by a time of order t_b and that a bubble of typical radius r_b is entrapped.

The above considerations, however, do not say how the time of formation of the jet t_j is affected by the gas cushioning. This sets constraints on the air-cushioning effect and we can *a priori* only turn to numerical simulations to see how the air layer dynamics interacts with jet formation. However, the previous analysis suggests two distinct regimes for the jet formation and thus for the value of t_j. More precisely, if $t_g \gg t_b$, which means that the jet forms after the bubble entrapment, one expects $t_j \sim t_g$. On the other hand, if $t_g \ll t_b$, the jet can only form after bubble entrapment so that $t_j \sim t_b$. These results evidence a transition from a regime where the gas thickness and cushioning effect are insignificant for the jet dynamics to a regime where the air cushioning controls the jet dynamics. This transition can be characterized by the ratio t_b/t_g and, provided that $\alpha = \rho_g/\rho_l$ is small enough, it defines a new dimensionless number J for the jet formation:

$$J = St^2\, Re^3 = \left(\frac{t_b}{t_g}\right)^3. \tag{2.33}$$

Therefore, $J \gg 1$ suggests that the jet forms just after the bubble entrapment while $J \ll 1$ would indicate that the bubble is entrapped much earlier than the time at which the jet is formed, creating potentially a number a secondary bubbles. The above considerations, however, do not say at what time t_j the liquid sheet is ejected. This sets constraints on the air-cushioning effect and we can only turn to numerical simulations to see how the air layer dynamics interacts with jet formation. Remarkably, $J = St^2\, Re^3 = Re\, \mu_g^2/\mu_l^2$ varies only with Re for a given liquid–gas pair, so it fixes a limiting $U_0 D$ for which the regime changes for a given pair of fluids. For an air–water system, for instance, taking $\mu_l/\mu_g \sim 50$ gives a transition at $Re \sim 3250$ or $U_0 = 3.25$ m s^{-1} for a $D = 1$ mm droplet and $\mu_l = 10^{-3}$ Pa s.

To conclude this scaling analysis, it is interesting to note that an alternative theory has been proposed recently (Klaseboer *et al.* 2014). There, a different scaling for the entrapment has been obtained (leading to $h_b \sim St^{1/2} D$ instead of $h_b \sim St^{2/3} D$) based on the balance between the lubrication pressure in the gas and the Bernoulli pressure in the drop $\rho_l U_0^2$. Although the pressure amplitude in numerical simulations of drop impact has been shown to obey the singular law (2.13), experimental studies have yet to distinguish between these two predictions.

3. Numerical method

In our continuum-mechanics modelling approach, fluid dynamics is Newtonian and incompressible, with constant surface tension. In the 'one-fluid approach' (Tryggvason, Scardovelli & Zaleski 2011) one considers a single fluid with variable viscosity and

density, and a singular surface tension force, yielding the Navier–Stokes equations

$$\rho\frac{\partial \boldsymbol{u}}{\partial t}+\rho\boldsymbol{\nabla}\cdot\boldsymbol{uu}=-\boldsymbol{\nabla}p+\boldsymbol{\nabla}\cdot\mu[\boldsymbol{\nabla u}+(\boldsymbol{\nabla u})^{\mathrm{T}}]+\sigma\kappa\boldsymbol{n}\delta_s, \tag{3.1}$$

$$\mathrm{div}(\boldsymbol{u})=0, \tag{3.2}$$

where $\boldsymbol{u}$ is the flow velocity, p is the pressure, $\boldsymbol{n}$ denotes the unit normal to the interface and δ_s is the 2-D Dirac distribution restricted to the interface and $\rho(x)$ and $\mu(x)$ are the space-dependent fluid densities and viscosities equal to their respective values $\rho_{l,g}$ and $\mu_{l,g}$ in each phase. This set of equations can be written using dimensionless variables, rescaling lengths by D, velocities by U_0, times by D/U_0, densities by ρ_l and pressures by $\rho_l U_0^2$ so that the Navier–Stokes equations become

$$\rho\frac{\partial \boldsymbol{u}}{\partial t}+\rho\boldsymbol{\nabla}\cdot\boldsymbol{uu}=-\boldsymbol{\nabla}\boldsymbol{p}+\boldsymbol{\nabla}\cdot\frac{\mu}{Re}[\boldsymbol{\nabla u}+(\boldsymbol{\nabla u})^{\mathrm{T}}]+\frac{\kappa}{We}\boldsymbol{n}\delta_s, \tag{3.3}$$

where now $\rho=\mu=1$ in the liquid phase while $\rho=\alpha=\rho_g/\rho_l$ and $\mu=\mu_g/\mu_l$ in the gas. Equation (3.3) is solved using the methods described in Popinet (2003, 2009), Lagrée, Staron & Popinet (2011) and Tryggvason *et al.* (2011), that is, by discretizing the fields on an adaptive quadtree grid using a projection method for the pressure, time stepping and the incompressibility condition. The advection of the velocity fields is performed using the second-order Bell–Collela–Glaz scheme, and momentum diffusion is treated partially implicitly. The interface is tracked using a volume of fluid (VOF) method with a mixed Youngs-centred scheme (Tryggvason *et al.* 2011) for the determination of the normal vector and a Lagrangian-explicit scheme for VOF advection. Curvature is computed using the height-function method. Surface tension is computed from curvature by a well-balanced continuous-surface-force method. Density and viscosity are computed from the VOF fraction C by an arithmetic mean. This arithmetic mean is followed by three steps of iteration of an elementary filtering. This whole set of methods is programmed either in the Gerris flow solver (Popinet 2016) or in the Gerris scripts that were designed to launch these computations.

Four refinement criteria are used as follows: (i) the local value of the vorticity; (ii) the presence of the interface as measured by the value of the gradient of the VOF 'colour function'; (iii) a measure of the error in the discretization of the various fields based on an *a posteriori* error estimate of a given field as a cost function for adaptation; this *a posteriori* error is estimated by computing the norm of the Hessian matrix of the components of the velocity field, estimated using third-order-accurate discretization operators; (iv) when near the interface, the curvature is used as the adaptation criterion. To measure the degree of refinement so obtained, recall that on a quadtree grid, a level of refinement n means that the grid cell is 2^n times smaller than the reference domain or 'box'. When adaptively refining, a predefined maximum level n_0 is used for the adaptation on curvature (iv); moreover, adaptation on vorticity (i) and on the error (iii) may lead to a maximum level of refinement n_0-1, and finally cells near the interface (ii) are always refined to level n_0-2 at the least. Note that criterion (iii) is generally more efficient than (i) so the latter could have been dropped altogether.

4. Results of simulations

4.1. *Impact dynamics*

We perform a series of simulations with parameters set as in table 1. To illustrate these values, for water-like fluids, these constant Weber and Froude numbers would

We	Fr	ρ_l/ρ_g	e/D	h_0/D
500	815	826.4	0.2	1/30

TABLE 1. Dimensionless values of the parameters for all simulations reported.

U_0	D	μ_l	μ_g	σ	e
4 m s^{-1}	2×10^{-3} m	4×10^{-3} kg m^{-1} s^{-1}	18×10^{-6} kg m^{-1} s^{-1}	64×10^{-3} kg s^{-2}	4×10^{-4} m

TABLE 2. Dimensional values of the main parameters for figure 1.

correspond to a 2 mm diameter drop falling at velocity 4 m s^{-1}. The numerical simulations are performed for different liquid and gas viscosities characterized by the Reynolds and Stokes numbers varying from 400 to 16 000 and from 5.65×10^{-7} to 2.26×10^{-5}, respectively. Again, for a 2 mm diameter drop impacting at 4 m s^{-1}, this would typically cover the range from one-eighth to twenty times the water viscosity, and from one-fourth to ten times the air viscosity. In particular, we have done most of the simulations for three Stokes numbers (2.26×10^{-6}, 9.05×10^{-6} and 2.26×10^{-5}) and a large range of Reynolds numbers (400, 600, 800, 1000, 2000, 4000, 8000 and 16 000) that will be used to analyse the dynamical properties of the impact.

In an initial phase the droplet falls undeformed until air-cushioning effects set in. Then, at some point in time the jet forms and a reconnection of the interfaces on the droplet and film occurs. Figure 1 shows a droplet impact with physical parameters approximating a glycerinated water droplet falling in air. The main dimensional parameters are given in table 2; other parameters approximate air at ambient temperature, leading to the dimensionless numbers $Re = 2000$ and $St = 2.26 \times 10^{-6}$ in complement to the dimensionless numbers of table 1.

The grid is refined based on the four criteria above so that the smallest cell has size $\Delta x = D/(3 \times 2^{13}) \sim D/25\,000$, corresponding to an effective refinement level of 15 in Gerris. Figure 3 shows two views of the grid refinement for a case where the liquid viscosity is twice as high as in table 2 and the gas density ten times larger, so that $Re = 1000$ and $St = 2.26 \times 10^{-6}$, all the other parameters being the same as in figure 1.

We have checked that higher h_0/D does not change the results significantly. This can also be verified from figure 4 where it can be seen directly that the simulation starts at a time $t_0 = -D/(30U_0)$, much larger than the apparent time scale of the air-cushioning effect. In fact, the velocity of the south pole of the droplet is unperturbed until very short times of approximately $t \sim -5 \times 10^{-3} D/U_0$.

In figures 1 and 4, one can observe that a bubble is indeed entrapped by the impact due to the cushioning of the gas beneath the droplet. A very thin ejecta sheet is formed, followed by the growth of a thicker corolla. These figures do not, however, give a full account of the level of accuracy reached in the calculation, as shown in figure 5, where successive zooms of the interface are presented around the instant when the droplet contacts the liquid film. The large range of scales between the droplet diameter and the small features in figure 5(*d*) is apparent, figure 3 showing the corresponding grid.

In particular, small bubbles (which are actually toroidal because of the axial symmetry) can be seen prior to the ejection of the thin liquid sheet. In this case, the liquid of the droplet has already made contact with the liquid layer before the

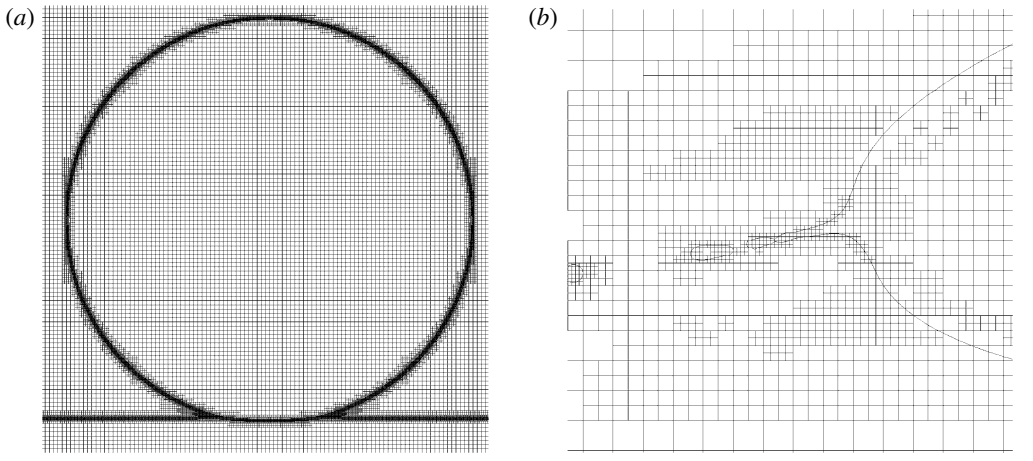

FIGURE 3. The grid refinement used in (*a*) figure 5(*a*) and (*b*) figure 5(*d*). Here, the viscosity is twice that of table 2, so that $Re = 1000$ with a gas viscosity such that $St = 2.26 \times 10^{-6}$ and $J = 0.005$.

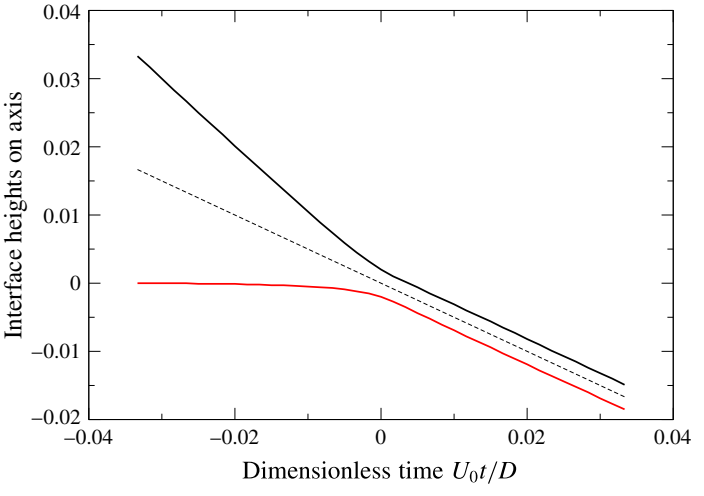

FIGURE 4. (Colour online) The dimensionless positions of the bottom of the droplet z_+/D and the top of the film on the axis z_-/D as functions of the dimensionless time U_0t/D for $St = 2.26 \times 10^{-5}$, $Re = 1000$ and thus $J = 0.5$. The dashed line represents the mean position that decreases like $-0.5U_0t$.

jet formation, which is consistent with the small value of the jet number $J = 0.005$. Indeed, after the first entrapment of the bubble, the jet cannot emerge from the connected interfaces so that additional bubbles are eventually entrapped by the dynamics. These small toroidal bubble entrapments might in fact correspond to those observed in experiments recently (Thoroddsen *et al.* 2012). However, this is also strongly controlled by the size of the grid, as reconnection in the VOF methods depends on the grid size, questioning these bubbles' existence in the continuum limit. In fact, a physical cutoff length is present in this problem, due to the mean

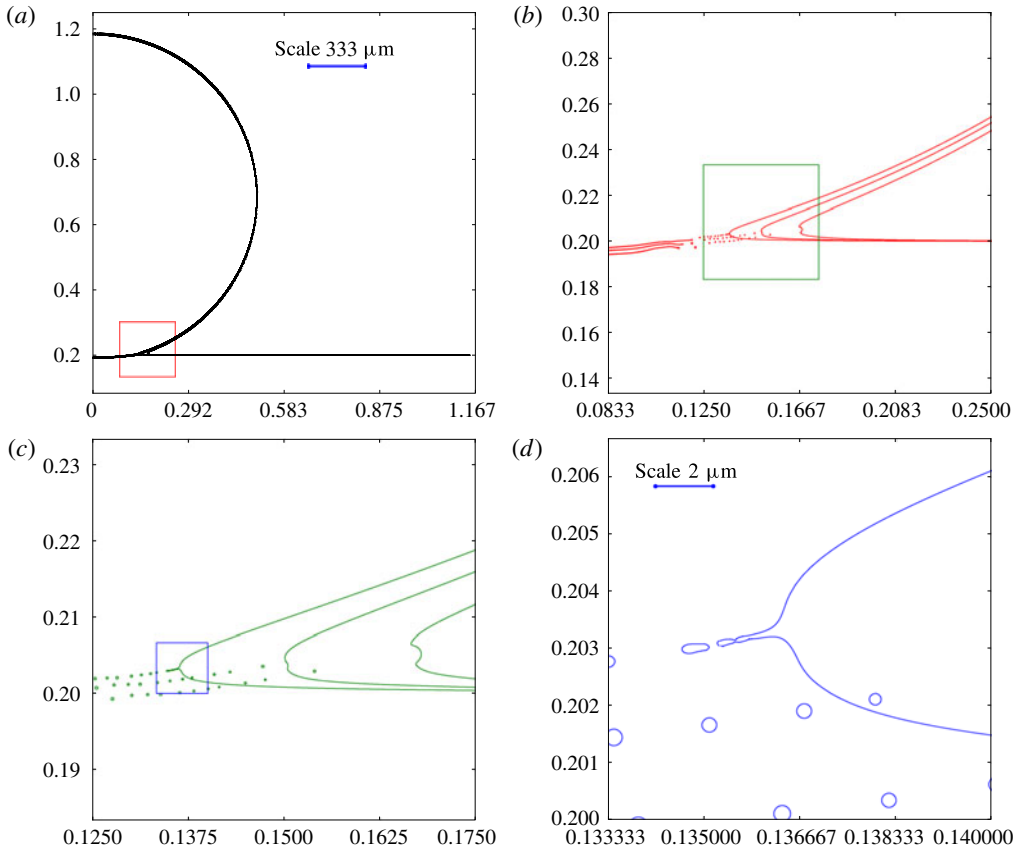

FIGURE 5. (Colour online) Successive zooms of the interface around the time of jet formation t_j for $Re = 1000$, $We = 500$ and $St = 2.26 \times 10^{-6}$ so that $J = 0.005$. (*a*) shows the general view; (*b*) shows the zoom of the interface corresponding to the square traced on (*a*), and so on from (*b*) to (*c*) and from (*c*) to (*d*). In the first and last figures, the physical scales are shown based on a $D = 2$ mm diameter drop for illustration. The 2 μm scale shown in the last figure corresponds in fact to twenty times the smallest mesh size of the numerical simulation. Remarkably, we observe a sequence of bubble entrapments before the jet is formed, in agreement with $J = (t_b/t_g)^3 \ll 1$.

free path in the gas under which the continuum mechanics is not valid and around which physical toroidal bubbles are eventually expected to form. Anyway, numerical simulations should not be performed at length scales below this cutoff. Considering again a $D = 2$ mm droplet for illustration, the finer grid size is $\Delta x \sim 8 \times 10^{-8}$ m, only one order of magnitude away from the molecular length scales. Thus, the VOF reconnection, although not yet physically realistic, may, in the future, approach the length scales at which molecular forces trigger reconnection in the real world. Finally, the mechanism of jet formation can be observed in figure 6, where the vorticity field in the liquid and gas phases is shown prior to the ejection corresponding to the zoom of figure 5(*d*). It exhibits a vortex dipole at the origin of the jet, as already described in JZ03.

In the following, we investigate the different quantities involved in the splashing dynamics as the liquid and gas viscosities vary.

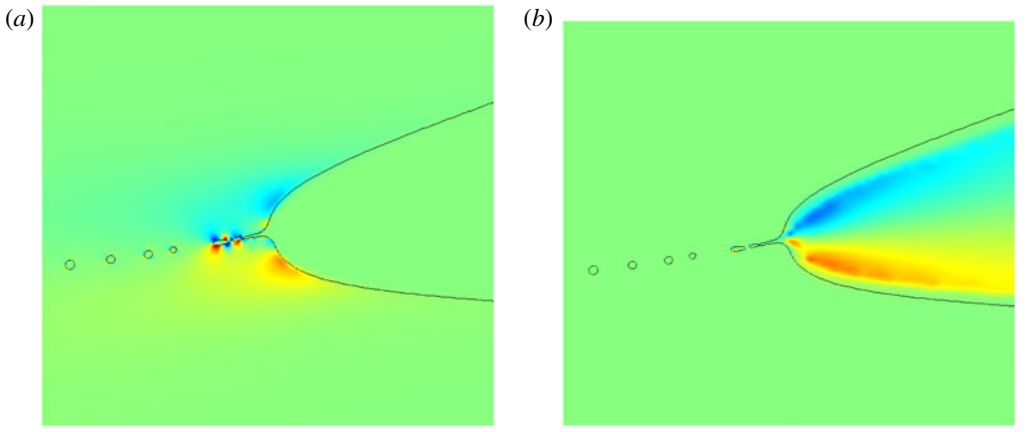

FIGURE 6. (Colour online) The vorticity field corresponding to figure 5(*d*): (*a*) in the liquid (the vorticity ranging here from −800 (blue) to 800 (red) in dimensionless units) and (*b*) in the gas (ranging from −2000 to 2000).

4.2. *Spreading radius*

One of the crucial quantities involved in the scaling analysis is the geometrical radius $r_g(t)$ that acts as the horizontal length scale. In order to verify that the horizontal scale behaves like $r_g(t)$, we investigate the evolution with time of the spreading radius, defined as the point in the liquid where the velocity is maximal. Figure 7 shows the evolution of the spreading radius with time for all the simulations performed. The square-root scaling ($r_g(t) = \sqrt{DU_0 t}$) is observed over a large range of time with the same prefactor for all simulations. Remarkably, the figure shows that this geometrical argument for the horizontal characteristic length is particularly robust and that the liquid properties (viscosities, densities) only influence the dynamics at short times.

4.3. *Initial gas sheet formation*

We now study the formation of the gas sheet and its scaling. The transition from free fall to air cushioning can be seen on the time history of the heights of the film and the bubble $z_-(r, t)$ and $z_+(r, t)$. Figure 4 shows both heights $z_-(0, t)$ and $z_+(0, t)$ on the axis as a function of time for $St = 2.26 \times 10^{-5}$ and $Re = 1000$. This corresponds to a value of the air viscosity 10 times its ordinary value, while the liquid is 8 times more viscous than water. It is seen that the heights behave linearly until some time near $t = 0$ (approximately $t \sim -5 \times 10^{-3} D/U_0$). The linear behaviour of $z_+(0, t)$ before impact is an indication that the bottom of the drop falls at the free fall velocity $U_0 + O(g(t - t_0))$ (the gravity correction is even smaller than Fr^{-1} due to the short time of observation) almost unperturbed from its initial value. At $t = 0$ on the other hand the cushioning dynamics has fully set in. After time 0, $z_+(0, t) \sim z_-(0, t) \sim -U_0 t/2$ and $z_+(0, t) - z_-(0, t)$ remains approximately constant. This half-velocity linear decrease of both $z_+(0, t)$ and $z_-(0, t)$ can be understood simply by momentum conservation as already suggested by Tran *et al.* (2013). The scale h_b of the gas layer may thus conveniently be defined as $h_b = z_+(0, 0) - z_-(0, 0)$.

To determine the scaling of h_b two series of simulations have been performed at $Re = 2000$ and $Re = 800$ for variable Stokes number St. Together with the numbers in table 1 these completely define the simulation parameters. The dimensionless height

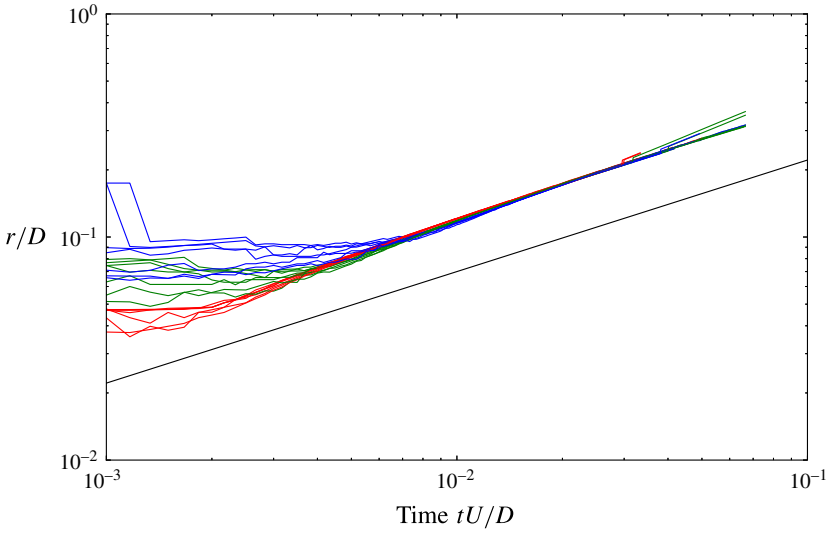

FIGURE 7. (Colour online) The dimensionless spreading radius, defined as the radius where the velocity is maximal in the liquid, as a function of the dimensionless time U_0t/D, in a log–log plot for all the simulations performed in this study. The straight line indicates the slope $1/2$ corresponding to the geometrical law $r_g = \sqrt{DU_0t}$ shifted below for eye guiding. As suggested by this geometrical relation, the different curves all collapse onto a single one parallel to the expected law, showing that viscous, capillary and lubrication effects only alter slightly this dynamics. Differences can, however, be seen at short times.

$\hat{h}_b = h_b/D$ is plotted in figure 8 together with relation (2.26). The unknown turbulent friction coefficient C_1 has been fitted by trial and error to $C_1 = 0.75 \pm 0.1$.

While the numerical data points are not exactly on top of the fit, the hypothesis of a transition from a $\hat{h}_b \to \hat{h}_{min} C_1\alpha$ limit at small St to a $\hat{h}_b \sim St^n$ behaviour at larger (but still small) St is compatible with the data, with n in some range around $2/3$. However, it is worth remarking that the rightmost part of the graph is closer to a $1/2$ power-law behaviour, suggesting that the alternative scenario proposed by Klaseboer *et al.* (2014) might be valid here. In order to test the scaling of $\hat{h}_b$ at very low St, when the effect of $\alpha = \rho_g/\rho_l$ is most marked, we show the results of a series of simulations at the smallest value of St available in our simulations in figure 8 with variable ρ_g/ρ_l, keeping all other numbers constant. The results are plotted in figure 9. We observe a linear increase of $\hat{h}_b$ with ρ_g/ρ_l, in agreement with the linear relation (2.29), with a constant in the limit $\rho_g/\rho_l \to 0$ that should depend on the Stokes number. Therefore, as the analysis on the pressure will confirm below, the alternative scaling of Klaseboer *et al.* (2014) is not valid here and $St^{1/2}$ has to be seen as a best-fit scaling in the intermediate regime between $\hat{h}_b\ C_1\alpha$ at low St and $\hat{h}_b \sim St^{2/3}$ at large St (Jian *et al.* 2015).

4.4. *Impact pressure*

In order to investigate quantitatively the various mechanisms involved in the impact dynamics and the jet formation, we follow the evolution in time of the maximum pressure on the axis in the gas layer in figure 10 for different Stokes numbers at constant $Re = 2000$, around the time of jet formation. We see a very large pressure

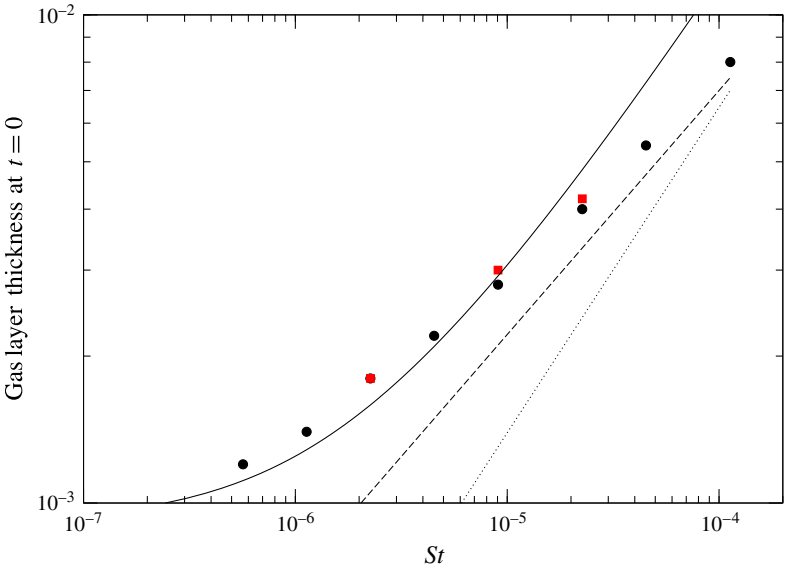

FIGURE 8. (Colour online) Height scale h_b/D of the gas layer as a function of the Stokes number for two values of the Reynolds number, $Re = 800$ (red squares) and $Re = 2000$ (black circles). The fit using equation (2.26) is shown (solid line) as well as the two scaling laws $St^{2/3}$ (dotted line) and $St^{1/2}$ (dashed line).

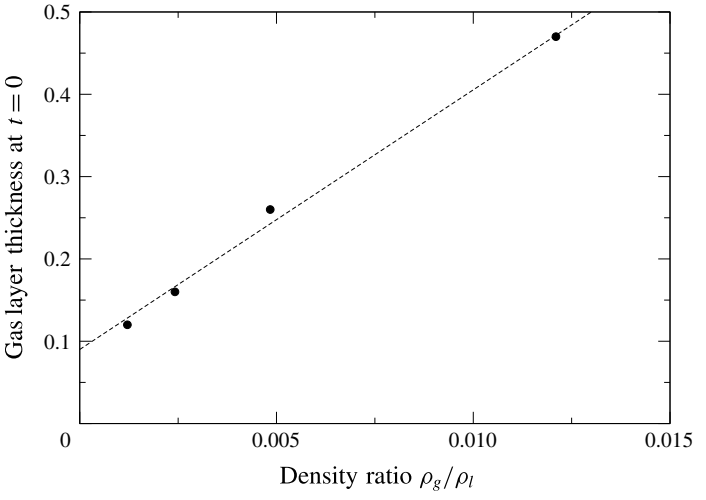

FIGURE 9. Height scale h_b/D of the gas layer as a function of ρ_g/ρ_l for $St = 5.67 \times 10^{-7}$ and $Re = 2000$ with all other parameters as in table 1.

peak at the formation of the jet, up to ten times the Bernoulli pressure $\rho_l U_0^2$ for the smallest St value. This peak is delayed and decreased as the St value increases. The insert of figure 10 plots the value of this peak pressure as a function of St, showing a very good agreement with the scaling $St^{-1/3}$ predicted in (2.32) by balancing the impact pressure of the drop with the lubrication pressure of the gas. This dependence of the pressure field on the Stokes number is clearly in disagreement with the

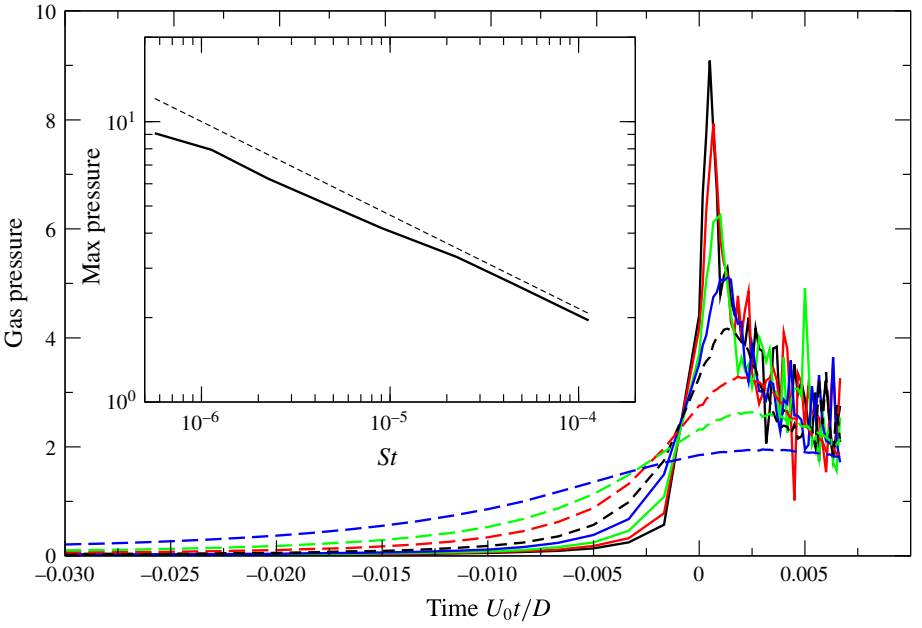

FIGURE 10. (Colour online) The pressure in the gas layer in the cushioning regime, defined as the maximum gas pressure on the axis down the drop. The dimensionless pressure (using $\rho_l U_0^2$) is plotted as a function of the dimensionless time U_0t/D for a fixed $Re = 2000$ and for varying Stokes number $St = 5.66 \times 10^{-7}$, 1.13×10^{-6}, 2.26×10^{-6}, 4.52×10^{-6}, 9.05×10^{-6}, 2.26×10^{-5}, 4.52×10^{-5} and 1.13×10^{-4}, from top to bottom. The insert shows the maximum pressure over time of these curves as a function of the Stokes number. The dashed line represents the expected $St^{-1/3}$ scaling following the prediction (2.32).

Bernoulli argument proposed in Klaseboer *et al.* (2014). Together with the variations of $\hat{h}_b$ described above, it indicates that the lubrication is the dominant regime in the air cushioning, in opposition to the alternative scenario of Klaseboer *et al.* (2014). We should also emphasize here that this high pressure in the gas layer can lead to compression of the gas, as happens for drop impact on a solid substrate (Mandre *et al.* 2009; Riboux & Gordillo 2014). Indeed, taking for instance the typical values for water drop impact $\rho_l = 1000$ kg m^{-3} and $U_0 \sim 4$ m s^{-3}, we obtain an additional pressure in the air of the order of three-fourths of the atmospheric pressure.

4.5. *Ejecta sheet velocity*

The ejecta sheet velocity can be measured by following the evolution of the velocity maximum in the liquid. This quantity is indeed an interesting proxy for several measurements and is easier and less ambiguous to measure than the ejecta thickness, which varies widely at its base. Figure 11 shows the maximum dimensionless velocity as a function of the dimensionless time shifted to the beginning of the simulation U_0t/D (remember that the origin of time $t = 0$ corresponds to the time at which the geometrical falling sphere would interact with the liquid layer), for $Re = 1000$ and $St = 9.05\,10^{-6}$, with other parameters defined in table 1. It is seen that the maximum velocity deviates from the initial velocity U_0 around $-U_0t_b/D \simeq -0.03$, that is, when

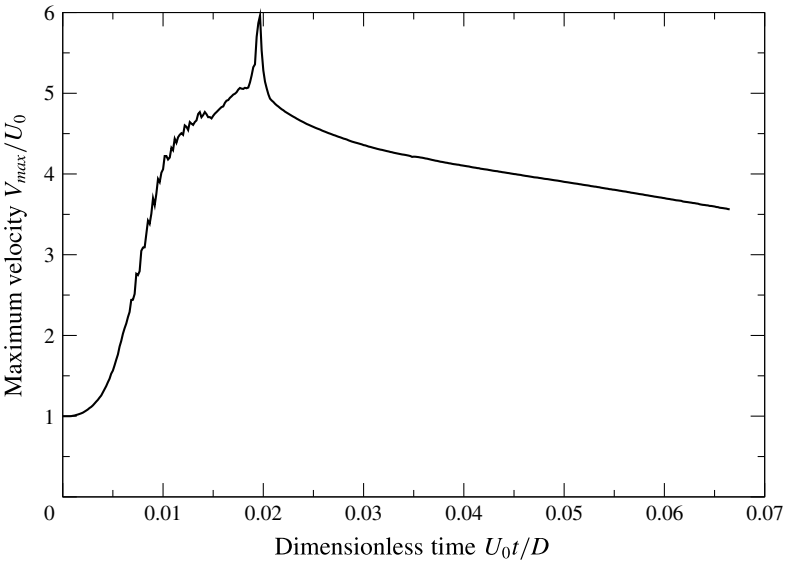

FIGURE 11. The maximum velocity V_{max}/U_0 as a function of the dimensionless time for $Re = 1000$ and $St = 9.05 \times 10^{-6}$, so that $J = 0.082$. Other parameters as in table 1.

the droplet approaches the liquid film, after which it increases rapidly, then reaches a maximum and decreases slowly. Finally, it has a tell-tale 'spike' at the instant of jet ejection marking t_j, the time of emergence of the ejecta sheet.

Indeed, figure 12 shows the value of the maximum velocity in the liquid and the location at which it is reached as time varies for the same parameters. It is clear in that case that the sharp peak corresponding to the maximum velocity also corresponds to the time of reversal of the curvature of the interface, marking the beginning of the ejection of the jet. Detailed investigations show that in all cases investigated in this paper, this spike corresponds exactly to the time of formation of the ejecta sheet, and that the maximum is located at its base.

However, zooming in on the base of the jet, as done in figure 5(*d*), shows that a set of tiny bubbles has already formed, meaning that first contact between the drop and the sheet has already occurred before the jetting time in figure 12. In other words, in this case, contact happens markedly before jet formation, in agreement with the small value of $J = 0.082$.

Defining the speed of the jet as this spike velocity, we can investigate how the jet velocity depends on the Reynolds numbers for the different Stokes numbers simulated. This velocity is shown in figure 13 as a function of the Reynolds number in order to check the validity of the scaling law (2.5): $U_j \propto \sqrt{Re}U_0$. The results are puzzling: indeed, while a reasonably good agreement for 'low' Reynolds numbers (below 1000) is observed, important deviations appear at larger Reynolds numbers where another scaling is apparently at play, consistent with a Re^n fit with $n \sim 1/5$. Moreover, it is interesting to notice that the jet velocity shows almost no dependence on the Stokes number below $Re \sim 1000$, as suggested by the viscous length theory of JZ03, while a small dependence can be identified in the higher-Reynolds-number regime.

In order to better understand this discrepancy between the predicted law and the numerical results, the dimensionless time $\hat{t}_j = U_0 t_j/D$ of the jet formation needs to

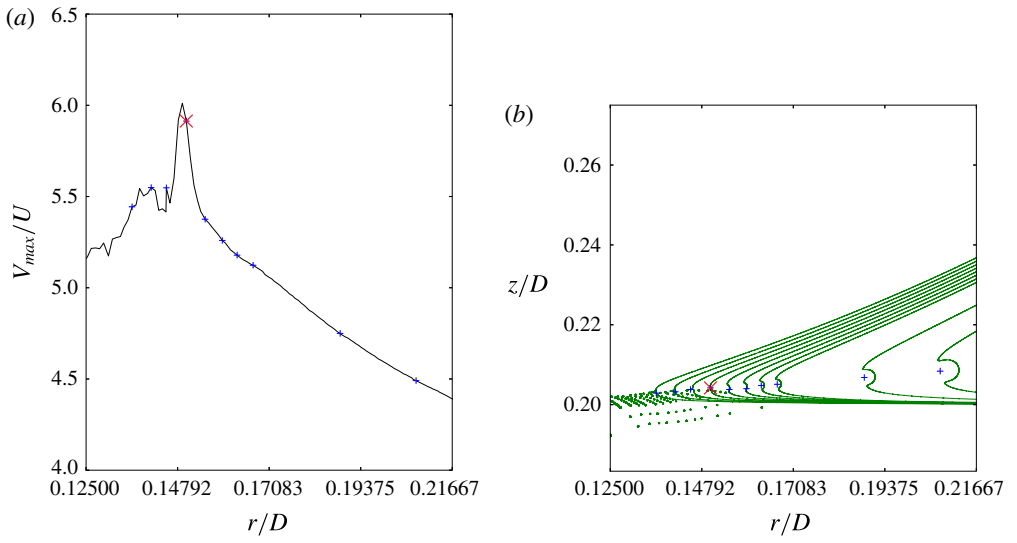

FIGURE 12. (Colour online) (*a*) Maximum velocity as a function of the radius where it is located for different times (indicated by the blue + signs). (*b*) Interface profiles corresponding to the same time. The position at which the velocity is maximum is again marked by blue + symbols. The location of the maximum velocity at time of reversal of the interface curvature, marking the beginning of jet ejection, is marked with a red × sign.

be investigated. Two scaling laws for this time are in competition, the ratio between these two time scales being quantified by the number J. On the one hand, the viscous length theory without accounting for the gas lubrication effect suggests that $\hat{t}_j \propto 1/Re$ (relation (2.6)); on the other hand, the cushioning of the gas suggests that this effect is delayed by the time $\hat{t}_b \sim St^{2/3}$ (relation (2.30)).

First of all, figure 14 exhibits parallel straight lines when plotting $\hat{t}_j$ as a function of $1/Re$ for three different Stokes numbers, indicating a linear relationship between $\hat{t}_j$ and $1/Re$. However, although the straight lines have similar slope, they have different origins for each Stokes number, suggesting that a time delay depending on the Stokes number has to be considered. This can be seen in figure 15 where $\hat{t}_j$ is plotted, for $Re = 2000$ as a function of $St^{2/3}$, as suggested by the theoretical law obtained for the bubble entrapment $\hat{t}_b$ (2.30).

Again, a good straight line is observed, demonstrating eventually that $\hat{t}_j$ obeys the following relation:

$$\hat{t}_j = A_1\, St^{2/3} + B_1\, Re^{-1}. \tag{4.1}$$

This relation can be written using the parameter J,

$$Re\,\hat{t}_j = A_1 J^{1/3} + B_1, \tag{4.2}$$

with A_1 and B_1 as fitting parameters. Figure 16 confirms this relation, by plotting $\hat{t}_j\, Re$ as a function of $J^{1/3}$ for all the simulations performed here. A good collapse of the data is obtained that is well fit by the formula (4.2) with $A_1 = 13.2$ and $B_1 = 14.5$.

The above study suggests that the impact dynamics can be decomposed into two dynamical stages: the first one is dominated by the cushioning dynamics involving a $St^{2/3}$ time scale dependence. Then, the ejection mechanism of the liquid sheet arises after a time delay proportional to $1/Re$.

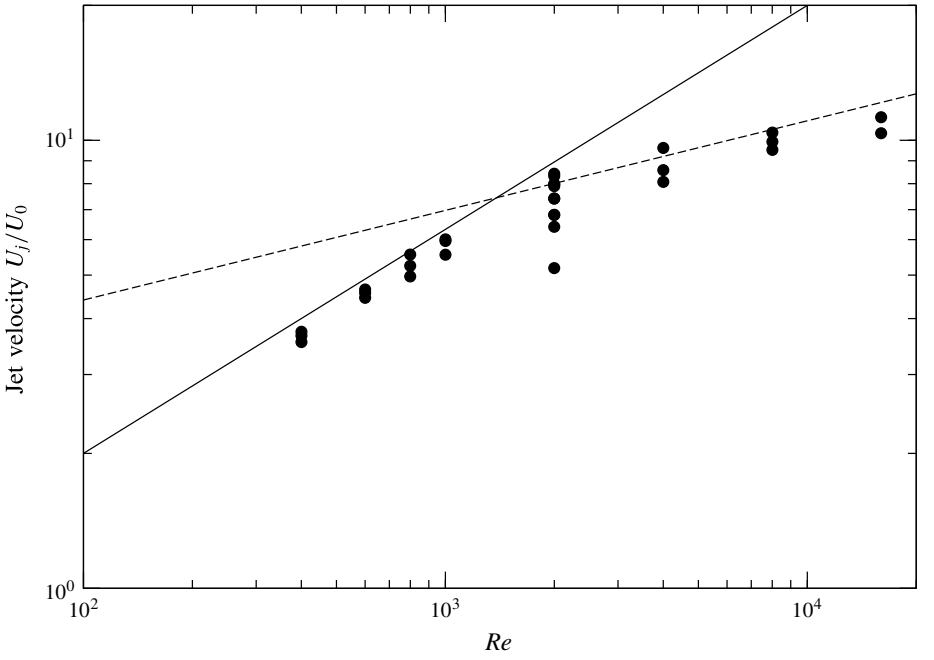

FIGURE 13. The jet velocities U_j/U_0 as a function of the Reynolds number for all the simulations performed in this study, in a log–log plot. The predicted power-law relation (2.5) is also plotted, showing only a reasonable agreement at Reynolds numbers lower than 1000 (solid line). For higher Reynolds numbers another scaling appears, consistent with a $Re^{1/5}$ law (dashed line). For $Re = 2000$, where many Stokes numbers have been considered, we note a slight dependence of the velocity on the Stokes number; the higher the Stokes number, the lower the jet velocity.

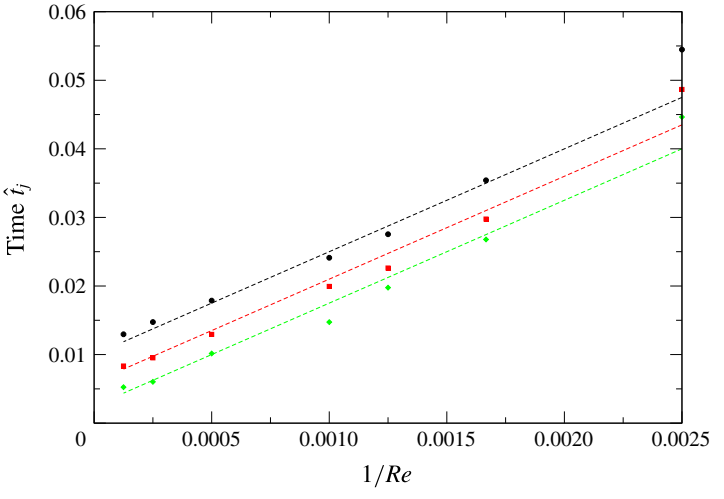

FIGURE 14. (Colour online) $\hat{t}_j = U_0 t_j/D$ as a function of the inverse of the Reynolds number ($1/Re$) for different Stokes numbers: black circles $St = 2.26 \times 10^{-5}$, red squares $St = 9.05 \times 10^{-6}$ and green diamonds $St = 2.26 \times 10^{-6}$. Parallel dashed straight lines are drawn for each Stokes number for guiding the eye.

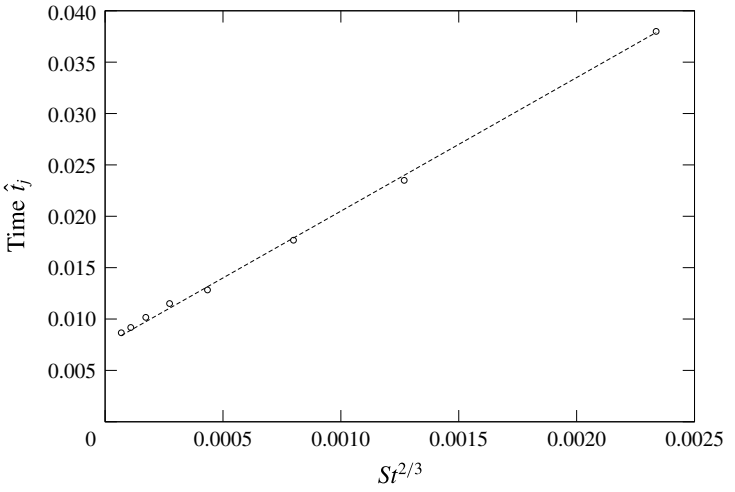

FIGURE 15. $\hat{t}_j$ as a function of the Stokes number to the power predicted by the theory (2.30), $St^{2/3}$, for constant Reynolds number $Re = 2000$. The dashed line indicates a linear relationship between these two quantities.

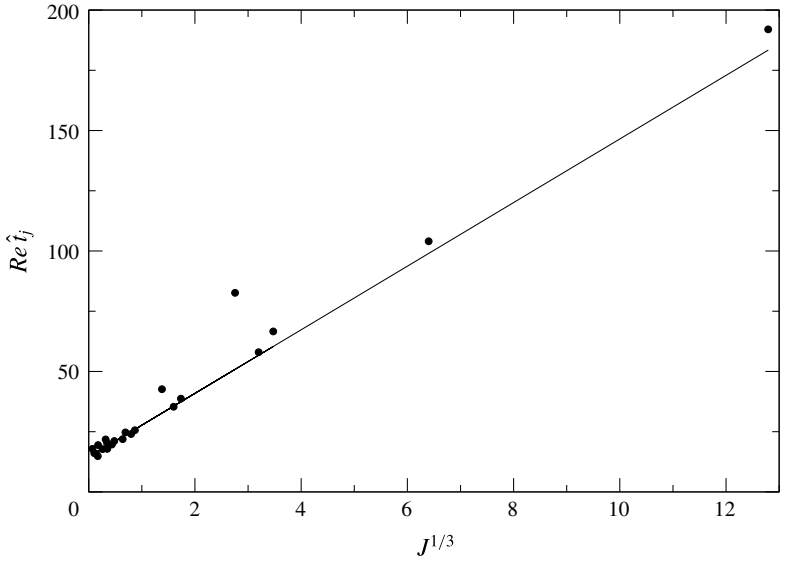

FIGURE 16. The data (black circles) for the jet formation time $Re\,\hat{t}_j$ plotted as a function of $J^{1/3}$ for all the simulations performed in this study. The data align almost perfectly along a line as suggested by the formula (4.2), which is used to fit the data (solid curve) using $A_1 = 13.2$ and $B_1 = 14.5$.

These different regimes can now be investigated through the evolution of the maximum velocity as function of time for all the parameters simulated here. Firstly, we show in figure 17(*a*) the maximum dimensionless velocity $\hat{V}_{max} = V_{max}/U_0$ as a function of the dimensionless time $\hat{t} = U_0 t/D$ for different Reynolds numbers and for a fixed Stokes number of $St = 2.26 \times 10^{-6}$, where it can be observed that the higher the

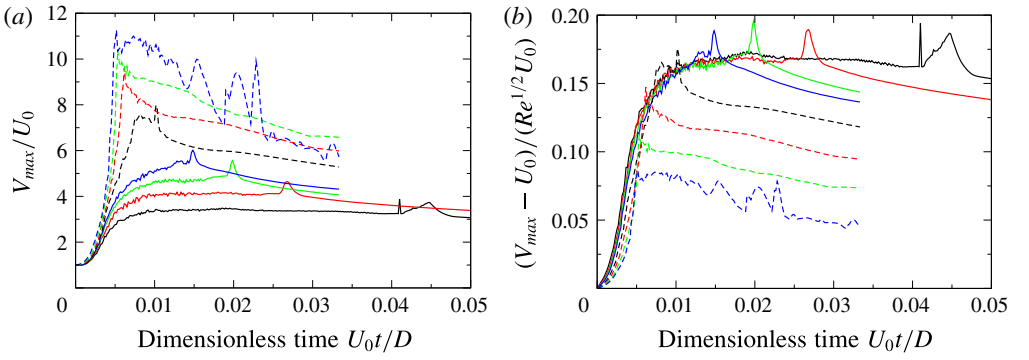

FIGURE 17. (Colour online) (*a*) Maximum velocity V_{max}/U_0 as a function of time for $St = 2.26 \times 10^{-6}$ and for various Reynolds numbers ($Re = 400$, 600, 800, 1000, 2000, 4000, 8000 and 16 000 for the curves from bottom to top). (*b*) Same curves where the velocity has been rescaled by the theoretical prediction $\sqrt{Re}$. In this case, the order of the curves for increasing Reynolds numbers is reversed, ranging from top to bottom. The initial velocity U_0 has been subtracted at short time for clarity.

Reynolds number, the higher is the velocity, as expected by the JZ03 prediction (2.5). This is investigated in figure 17(*b*), where these dimensionless velocities are rescaled by the predicted scaling $\sqrt{Re}$ and plotted as a function of time. If a reasonable collapse of the curve is obtained, firstly at short times and for Reynolds numbers below 1000, the curves for higher Reynolds numbers deviate from the master curve starting at the dimensionless time $\hat{t}_j$ of the jet formation. As expected, however, the time $\hat{t}_j$ decreases as the Reynolds number increases, but for the high Reynolds numbers, the velocity peak appears during the velocity rise, indicating that eventually the two mechanisms of air cushioning and jet formation interact. Somehow, the air-cushioning effect is interrupted by the ejection of the liquid sheet. This explains why the jet velocity at high Reynolds number does not follow the prediction (2.5). On the other hand, for lower Reynolds numbers (and hence lower jet numbers J), one can see that the two mechanisms of air cushioning and jet formation are well separated in time.

The dependence of the dynamics on the Stokes numbers can be observed in figure 18(*a*) where the maximum velocity V_{max}/U_0 is shown at $Re = 2000$ for different Stokes numbers. As expected by lubrication theory, the higher the Stokes number the slower the rise of the velocity. On the other hand, since the formation of the jet is delayed by this cushioning dynamics, we observe that the velocity peak is also delayed and is slightly decreasing as the Stokes number increases. This is in contradiction with the JZ03 initial prediction (2.5) that was obtained by neglecting the gas cushioning, explaining why this relation is not verified. The velocity curves are rescaled in figure 18(*b*) by $\sqrt{Re}$ as suggested by the prediction (2.5) for three Stokes numbers and different Reynolds numbers (up to 8 for a given Stokes number). The curves are arranged in three sets (one for each Stokes number for all the Reynolds numbers) in time, showing clearly that the Stokes number influences mostly the accelerating regime. The $\sqrt{Re}$ predicted scaling for the jet velocity is seen from the maximum of these curves, which are very close to each other. However, as observed in the jet velocity curve shown in figures 13 and 17, many curves do not reach this maximum because of the cushioning dynamics.

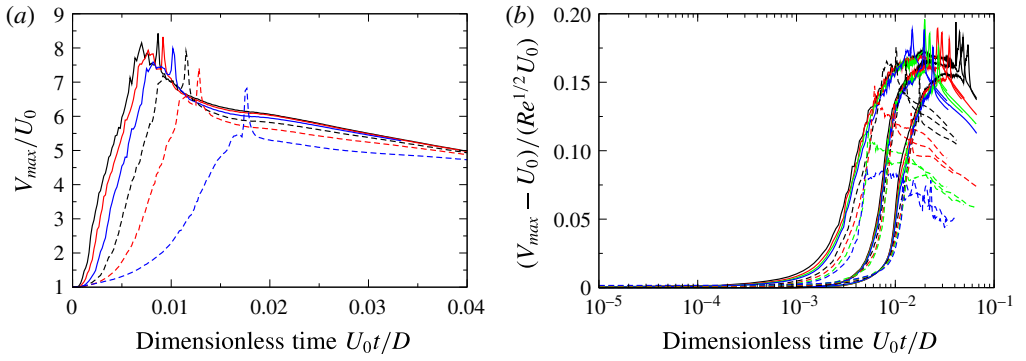

FIGURE 18. (Colour online) (*a*) Maximum velocity V_{max}/U_0 as a function of time for $Re = 200$ and for various Stokes numbers ($St = 5.65 \times 10^{-7}$, 1.13×10^{-6}, 2.26×10^{-6}, 4.52×10^{-6}, 9.05×10^{-6} and 2.26×10^{-5} for the curves from left to right). (*b*) For three Stokes numbers 2.26×10^{-6}, 9.05×10^{-6} and 2.26×10^{-5} the maximum velocity rescaled by $\sqrt{Re}$ are shown for different Reynolds numbers ranging from 400 to 16 000, in a log–linear plot. Three sets of curves can be identified, one for each Stokes number, from left to right as the Stokes number increases. Here, the initial velocity U_0 has been subtracted at short time for clarity.

The curves for the three Stokes numbers in figure 18 result in three different curves which are roughly translated on the logarithmic time axis, suggesting a scaling dependence on the Stokes number. The cushioning being characterized by the bubble entrapment time t_b, it is tempting to rescale the time by t_b, which scales at first order like $U_0t/(D\,St^{2/3})$. In fact, the best rescaling of the curve is obtained using the precise dependence of t_b on the Stokes number involving the inertial correction, formula (2.31), as shown in figure 19. There, a very good collapse of all the curves simulated in the study is obtained, showing that the jet rise follows cushioning dynamics. These results suggest that in this first dynamical stage, where the air cushioning is dominant, the velocity obeys the following relation (taking the first-order approximation $\hat{t}_b \sim St^{2/3}$):

$$V_{max} \sim \sqrt{Re}\,U_0 f_c[(U_0t/D)\,St^{-2/3}], \tag{4.3}$$

using here as a first-order approximation $\hat{t}_b \sim St^{2/3}$; f_c is the universal function that describes this cushioning regime. Immediately after the jet formation, and in a kind of plateau region, the velocity at the base of the jet does scale with $Re^{1/2}$ for intermediate Reynolds numbers, as predicted by (2.5), while it departs slightly from this scaling for high Reynolds numbers. Although this evolution is in agreement with the initial theory of JZ03, it is important to note that the velocity is not constant and is in fact decreasing with time after the jet formation time t_j. This second stage is determined by the jet dynamics and is *a priori* not influenced by the surrounding gas. Recalling that the time scale for the jet formation in the absence of gas cushioning is $t_g \sim D/(Re\,U_0)$, it is tempting to investigate the evolution with time of the maximum velocity as a function of the rescaled time $t/t_g = Re\,U_0t/D$, following

$$V_{max} \sim \sqrt{Re}\,U_0 f_j(Re\,U_0t/D), \tag{4.4}$$

where f_j is the universal function describing this second dynamical stage. The rescaled velocities $V_{max}/\sqrt{Re}\,U_0$ are shown in figure 20 as a function of the rescaled time

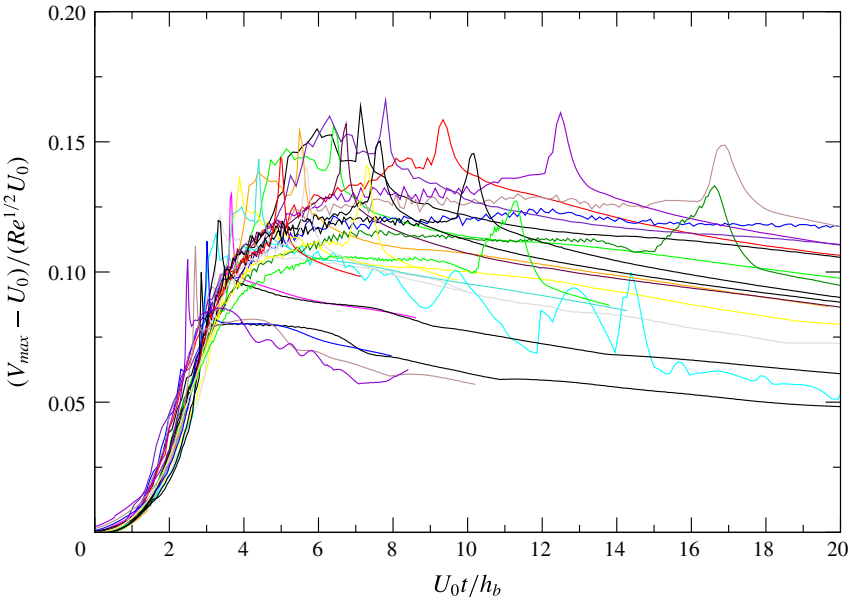

FIGURE 19. (Colour online) Rescaled velocities by $\sqrt{Re}$ for all the simulations performed in this study as a function of the rescaled time (t/t_b), where t_b is computed using formula (2.31). The initial velocity U_0 has been subtracted at short time for clarity.

$Re\, U_0 t/D$ for all the simulations performed in this study. Remarkably, a good collapse of the curves is observed for the large-time dynamics, i.e. for the time after the jet formation ($t > t_j$). The dashed line in this log–log plot exhibits a good fit of the data in this regime, using a $-3/10$ power law, so that the maximum velocity obeys eventually for $t > t_j$:

$$V_{max} \sim \sqrt{Re}\, U_0 f_j(Re\, U_0 t/D) \sim \sqrt{Re}\, U_0 \left(\frac{Re U_0 t}{D}\right)^{-3/10}. \tag{4.5}$$

This behaviour suggests an explanation for the selection of the maximum jet velocity, considering that this latter regime starts at the jetting time t_j. Recall first the asymptotic scalings observed for the jet maximum velocity shown in figure 13, namely $V_{max} \sim \sqrt{Re}\, U_0$ for $Re \leqslant 1000$ and $V_{max} \sim Re^{1/5} U_0$ otherwise. Interestingly, these two asymptotics are consistent with the function f_j (4.5) when considering the two asymptotics for the jet formation time t_j. Indeed, for $Re \leqslant 1000$ we have $t_j \sim D/(Re\, U_0)$ so that, using (4.5), the first scaling is $V_{max} \sim \sqrt{Re}\, U_0$. On the other hand, in the other regime, $Re \geqslant 1000$, for which $t_j \sim St^{2/3} D/U_0$, we obtain

$$V_{max} \sim \sqrt{Re}\, U_0 (Re\, St^{2/3})^{-3/10} \sim Re^{1/5}\, St^{-1/5}, \tag{4.6}$$

giving, remarkably, the velocity scaling for large Reynolds numbers. Note also that it predicts a power-law dependence on the Stokes number that we have not tested so far, although it can be qualitatively seen in figure 13. Finally, using the formula (4.2) for $\hat{t}_j$,

$$Re\, \hat{t}_j = A_1 J^{1/3} + B_1, \tag{4.7}$$

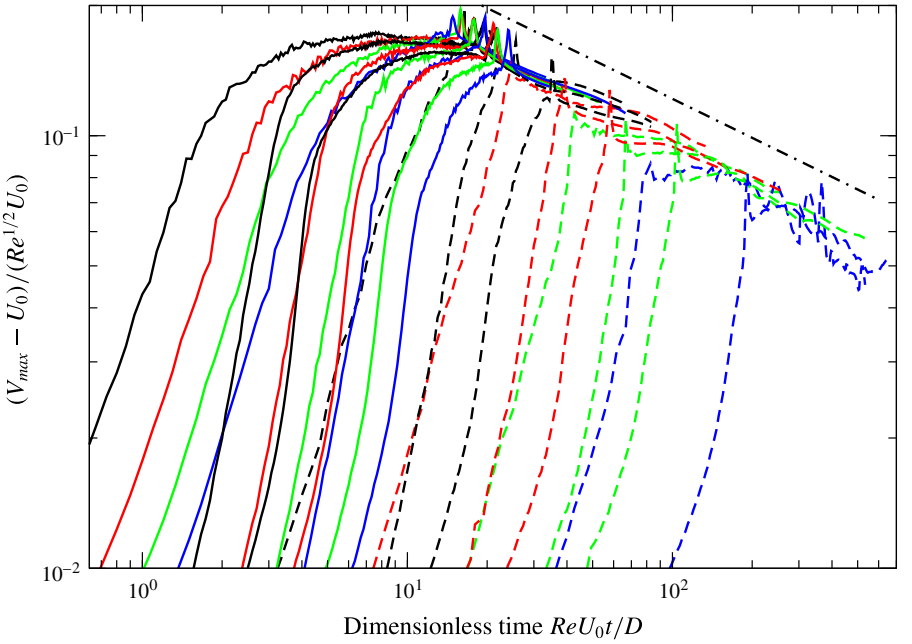

FIGURE 20. (Colour online) The rescaled maximum velocity $V_{max}/(\sqrt{Re}\,U_0)$ shown as a function of the rescaled time $Re\,U_0t/D$ based on the geometrical time scale for jet ejection t_g (see relation (2.6)) in a log–log plot. The dot-dashed line indicates the power-law scaling $(Re\,U_0t/D)^{-3/10}$. The initial velocity U_0 has been subtracted at short time for clarity.

and formula (4.5), we obtain an effective formula for the maximum jet velocity:

$$\frac{V_{max}}{\sqrt{Re}} = C_1 \frac{U_0}{(A_1 J^{1/3} + B_1)^{3/10}}, \tag{4.8}$$

where the initial theoretical law of JZ03 $V_{max} \propto \sqrt{Re}\,U_0$ is corrected by the cushioning dynamics quantified by the number J.

This formula is tested in figure 21 where the measured jet velocity for all the numerical simulations performed here, rescaled by the factor $U_0/(A_1J^{1/3} + B_1)^{3/10}$, is plotted as a function of the Reynolds number, showing the validity of the formula (4.8).

4.6. *Bubble entrapment versus jet formation?*

We have observed in our simulations that, in most cases, the jet emergence is simultaneous with the connection of the two interfaces, that is, the bubble becomes trapped at the time of jet formation. In fact, the situation is more complex and can be analysed using the jet number J that quantifies the transition between a regime where the air cushioning is insignificant ($J \ll 1$) and a regime where it is dominant ($J \gg 1$). When the air cushioning is insignificant, we find that the jet forms at the geometrical time $t_g \gg t_b$ (recall that $J = t_b^3/t_g^3$), with a jet velocity of the order of $Re^{1/2}$, as predicted earlier in JZ03. Moreover, we find that this velocity scale is present before jet formation, indicating the existence of a large velocity in the droplet prior to the formation of the jet. This large velocity (asymptotically infinitely larger than U_0) is indicative of the focusing of the liquid velocity in a small region inside the droplet

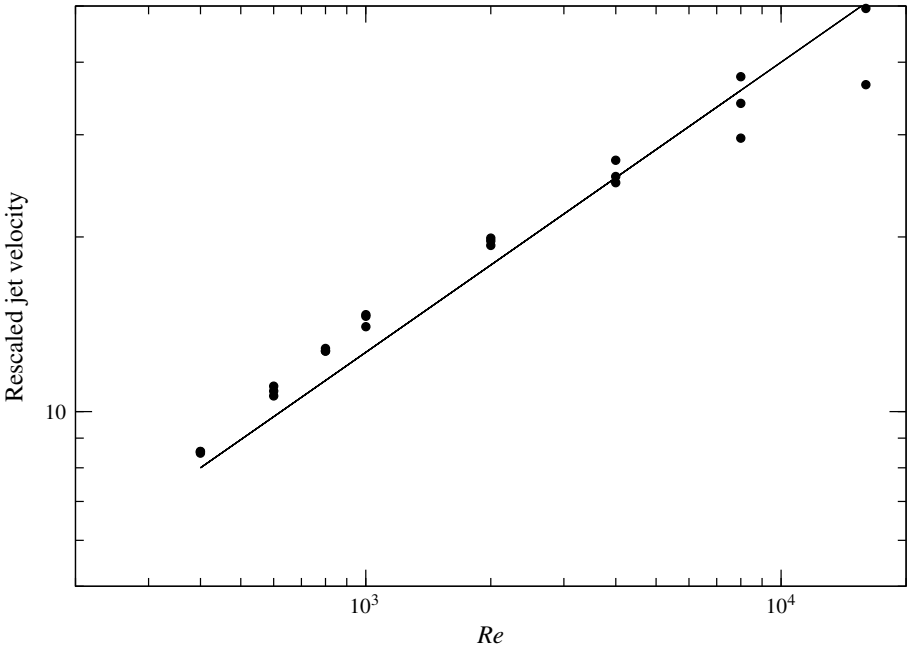

FIGURE 21. Black circles: the numerically measured jet velocity rescaled by the dependence in the J number following formula (4.8), $(A_1 J^{1/3} + B_1)^{3/10} U_j/U_0$, as a function of the Reynolds number. The $\sqrt{Re}$ law is drawn (solid line) showing the validity of (4.8) using $C_1 = 0.4$.

prior to the emergence of the jet. In this regime, where the gas cushioning effect is insignificant, the first bubble entrapment occurs before jet formation. A trace of this is seen in the presence of the small bubbles in figure 5(*d*) before jet formation. This is even clearer in figure 22, which shows the details of the interface dynamics between the time of first contact between the drop and the liquid film and the formation of the jet, for $Re = 2000$ and $St = 5.66 \times 10^{-7}$, leading to $J = 2.56 \times 10^{-3}$. After the first contact between the drop and the liquid layer, no jet can form since $t_b \ll t_g$, so additional bubbles (toroidal here because of the axial symmetry) are entrapped by the falling drop before the jet can eventually escape the falling droplet.

We observe that a delay exists between the first connection of the interfaces (figure 22*a*) and the jet formation (figure 22*d*), during which small bubbles are entrapped by the thin gas film dynamics.

On the other hand, in the regime where J is large (and similarly $t_b \gg t_g$) it is not clear how jet formation and air bubble entrapment interact, but one expects that no small bubbles are entrapped and that the jet is formed simultaneously to the bubble entrapment. This is illustrated in figure 23 for $Re = 16\,000$ and $St = 2.26 \times 10^{-7}$, so that $J = 2700$, where the jet expands as soon as the drop and the liquid layer have merged.

5. Conclusion

In our numerical experiments, we have focused on the jet velocity and the effect of the gas layer on the impact of a droplet onto a thin film of the same liquid. The formation and the scaling of the gas layer were analysed. As the gas layer cushions

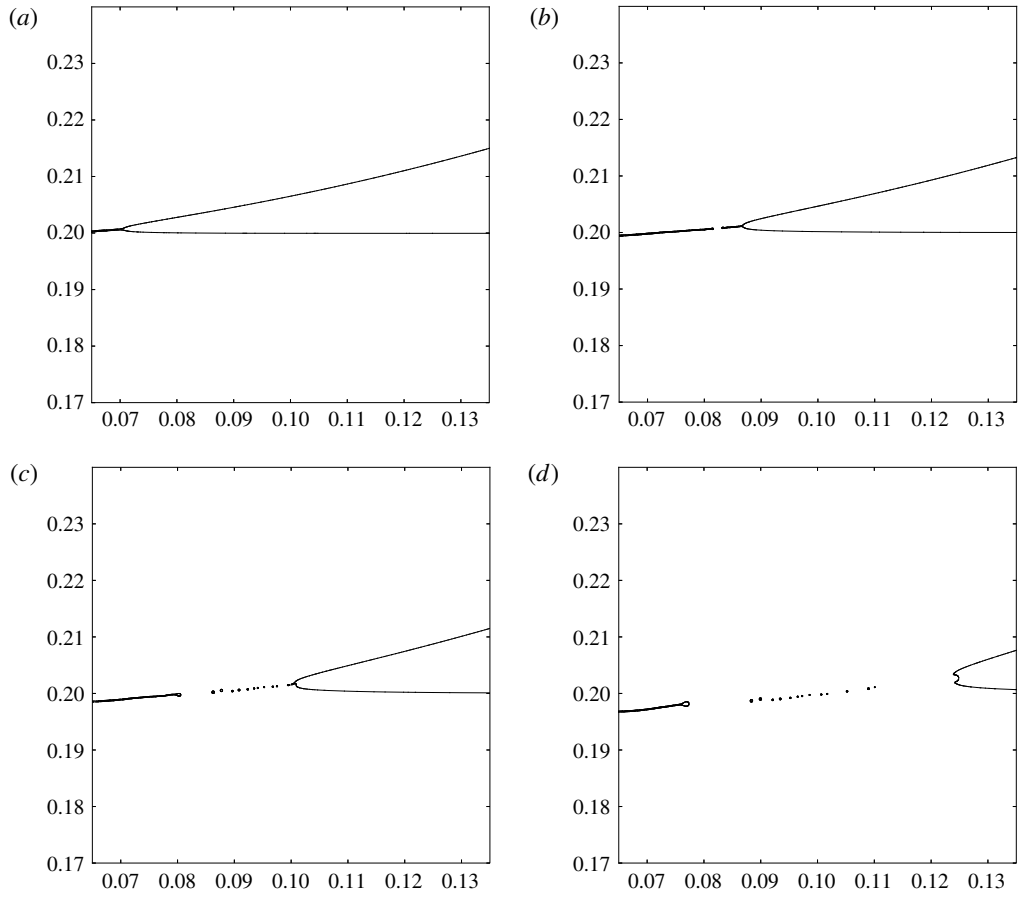

FIGURE 22. Zoomed-in pictures of the connection of the upper interface of the drop with the liquid layer for $Re = 2000$ and $St = 5.66 \times 10^{-7}$, the other parameters being those of table 1. The interfaces are shown at times $U_0 t/D = 3.67 \times 10^{-3}$ (*a*), 5.33×10^{-3} (*b*), 7×10^{-3} (*c*) and 1.03×10^{-2} (*d*). The jet number $J = 2.56 \times 10^{-3} \ll 1$ and we thus observe that after the first connection of the two interfaces in (*a*), small bubbles are created at the front of the connection by the retraction of the thin gas layer that is still between the falling drop and the liquid film, (*b*) and (*c*), until the jet emerges on (*d*). On the other side of the connected region, the thin air film forming the entrapped large bubble is also retracting by capillarity.

the impact, a large peak in pressure is observed which scales like $P_{imp} \sim \rho_l U_0^2 \, St^{-1/3}$, as predicted by lubrication theory, leading eventually to bubble entrapment. The formation of the gas layer itself shows interesting symmetry properties between the dynamics of the droplet surface z_+ and the dynamics of the liquid layer z_-. The two are equally deformed at the time $t = 0$. The time during which deformation sets up is very short compared to the characteristic time D/U_0 and also to the time of free fall h_0/U_0. The corresponding layer thickness exhibits an intermediate regime between the $D\,St^{2/3}$ scaling outlined by lubrication theory and an inertial regime independent of the Stokes number at low St, confirming that the dominant mechanism for the air cushioning is determined by the lubrication regime. The dependence of the layer thickness shows in addition a linear relationship with the density ratio ρ_g/ρ_l (figure 9), as predicted by theory (2.29).

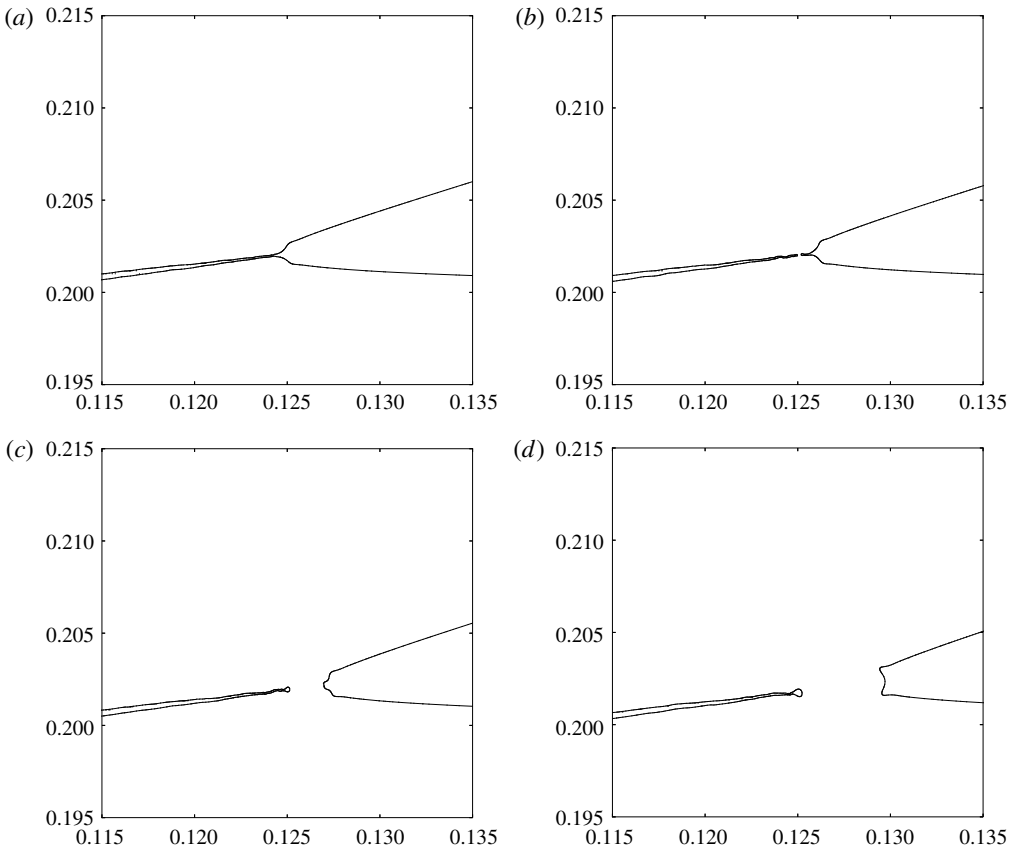

FIGURE 23. Zoomed-in pictures of the connection of the upper interface of the drop with the liquid layer for $Re = 16\,000$ and $St = 2.26 \times 10^{-5}$, the other parameters being those of table 1. The interface is shown at times $U_0 t/D = 0.01167$ (*a*), 0.01182 (*b*), 0.012 (*c*) and 0.0123 (*d*). The jet number $J = 2700 \gg 1$ and the first connection of the two interfaces occurs between (*a*) and (*b*). No additional bubbles are entrapped and the jet is directly emerging from this connection, (*d*).

The results for the jetting time t_j exhibit another interplay between the gas cushioning (whose time scale is determined by $St^{2/3}$, neglecting as a first approximation the inertial correction) and the liquid viscous boundary layer mechanism described in JZ03 (with a time scale of $1/Re$). This interplay is very well described by the new dimensionless parameter $J = St^2 Re^3$ introduced in this work. This number J characterizes indeed the influence of the gas cushioning on the splashing dynamics. At large J, the jet formation is delayed by the bubble entrapment, while at small J, a rosary of bubbles is formed before the liquid jet can emerge. Finally, we have shown here that these coupled mechanisms explain how the jet velocity varies with the impact parameters.

REFERENCES

AGBAGLAH, G. & DEEGAN, R. 2014 Growth and instability of the liquid rim in the crown splash regime. *J. Fluid Mech.* **752**, 485–496.

AGBAGLAH, G., THORAVAL, M.-J., THORODDSEN, S., ZHANG, L., FEZZAA, K. & DEEGAN, R. 2015 Drop impact into a deep pool: vortex shedding and jet formation. *J. Fluid Mech.* **764**, R1.

CULICK, F. E. C. 1960 Comments on a ruptured soap film. *J. Appl. Phys.* **31**, 1128–1129.

DEEGAN, R., BRUNET, P. & EGGERS, J. 2008 Complexities of splashing. *Nonlinearity* **21**, C1.

DUCHEMIN, L. & JOSSERAND, C. 2011 Curvature singularity and film-skating during drop impact. *Phys. Fluids* **23**, 091701.

FUSTER, D., AGBAGLAH, G., JOSSERAND, C., POPINET, S. & ZALESKI, S. 2009 Numerical simulation of droplets, bubbles and waves: state of the art. *Fluid Dyn. Res.* **41**, 065001.

GUEYFFIER, D. & ZALESKI, S. 1998 Formation de digitations lors de l'impact d'une goutte sur un film liquide. *C. R. Acad. Sci. Paris* II **326**, 839–844.

HICKS, P. & PURVIS, R. 2010 Air cushioning and bubble entrapment in three-dimensional droplet impacts. *J. Fluid Mech.* **649**, 135–163.

HICKS, P. & PURVIS, R. 2011 Air cushioning in droplet impacts with liquid layers and other droplets. *Phys. Fluids* **23**, 062104.

HICKS, P. & PURVIS, R. 2013 Liquid–solid impacts with compressible gas cushioning. *J. Fluid Mech.* **735**, 120–149.

HOWISON, S., OCKENDON, J., OLIVER, J., PURVIS, R. & SMITH, F. 2005 Droplet impact on a thin fluid layer. *J. Fluid. Mech.* **542**, 1–23.

JIAN, Z., JOSSERAND, C., RAY, P., DUCHEMIN, L., POPINET, S. & ZALESKI, S. 2015 Modelling the thickness of the air layer in droplet impact. In *ICLASS 2015, 13th Triennial International Conference on Liquid Atomization and Spray Systems (Tainan, Taiwan, 23–27 August 2015)*.

JOSSERAND, C. & THORODDSEN, S. 2016 Drop impact on a solid surface. *Annu. Rev. Fluid Mech.* **48**, 365–391.

JOSSERAND, C. & ZALESKI, S. 2003 Droplet splashing on a thin liquid film. *Phys. Fluids* **15**, 1650.

KLASEBOER, E., MANICA, R. & CHAN, D. Y. 2014 Universal behavior of the initial stage of drop impact. *Phys. Rev. Lett.* **113** (19), 194501.

KOLINSKI, J. M., RUBINSTEIN, S. M., MANDRE, S., BRENNER, M. P., WEITZ, D. A. & MAHADEVAN, L. 2012 Skating on a film of air: drops impacting on a surface. *Phys. Rev. Lett.* **108**, 074503.

KOROBKIN, A., ELLIS, A. & SMITH, F. 2008 Trapping of air in impact between a body and shallow water. *J. Fluid Mech.* **611**, 365–394.

LAGRÉE, P. Y., STARON, L. & POPINET, S. 2011 The granular column collapse as a continuum: validity of a two-dimensional Navier–Stokes model with a μ(I)-rheology. *J. Fluid Mech.* **686**, 378–408.

LESSER, M. & FIELD, J. 1983 The impact of compressible liquids. *Annu. Rev. Fluid Mech.* **15**, 97–122.

LUCHINI, P. & CHARRU, F. 2010 Consistent section-averaged equations of quasi-one-dimensional laminar flow. *J. Fluid. Mech.* **565**, 337–341.

MANDRE, S. & BRENNER, M. 2012 The mechanism of a splash on a dry solid surface. *J. Fluid Mech.* **690**, 148–172.

MANDRE, S., MANI, M. & BRENNER, M. 2009 Precursors to splashing of liquid droplets on a solid surface. *Phys. Rev. Lett.* **102**, 134502.

MANI, M., MANDRE, S. & BRENNER, M. 2010 Events before droplet splashing on a solid surface. *J. Fluid Mech.* **647**, 163–185.

MEHDI-NEJAD, V., MOSTAGHIMI, J. & CHANDRA, S. 2003 Air bubble entrapment under an impacting droplet. *Phys. Fluids* **15** (1), 173–183.

MUNDO, C., SOMMERFELD, M. & TROPEA, C. 1995 Droplet-wall collisions: experimental studies of the deformation and breakup process. *Intl J. Multiphase Flow* **21**, 151–173.

PHILIPPI, J., LAGRÉE, P.-Y. & ANTKOWIAK, A. 2016 Drop impact on solid surface: short time self-similarity. *J. Fluid Mech.* **795**, 96–135.

POPINET, S. 2003 Gerris: a tree-based adaptive solver for the incompressible euler equations in complex geometries. *J. Comput. Phys.* **190** (2), 572–600.

POPINET, S. 2009 An accurate adaptive solver for surface-tension-driven interfacial flows. *J. Comput. Phys.* **228**, 5838–5866.

POPINET, S. 2016 Gerris flow solver, http://gfs.sourceforge.net/.

REIN, M. 1993 Phenomena of liquid drop impact on solid and liquid surfaces. *Fluid Dyn. Res.* **12**, 61–93.

RIBOUX, G. & GORDILLO, J. 2014 Experiments of drops impacting a smooth solid surface: a model of the critical impact speed for drop splashing. *Phys. Rev. Lett.* **113**, 024507.

RIEBER, M. & FROHN, A. 1998 Numerical simulation of splashing drops. In *Proceedings of ILASS98, Manchester*, Academic Press.

RIOBOO, R., MARENGO, M. & TROPEA, C. 2001 Outcomes from a drop impact on solid surfaces. *Atomiz. Sprays* **11**, 155–165.

STOW, C. & HADFIELD, M. 1981 An experimental investigation of fluid flow resulting from the impact of a water drop with an unyielding dry surface. *Proc. R. Soc. Lond.* A **373**, 419–441.

TAYLOR, G. I. 1959 The dynamics of thin sheets of fluid III. Disintegration of fluid sheets. *Proc. R. Soc. Lond.* A **253**, 313–321.

THORAVAL, M.-J., TAKEHARA, K., ETOH, T., POPINET, S., RAY, P., JOSSERAND, C., ZALESKI, S. & THORODDSEN, S. 2012 von Kármán vortex street within an impacting drop. *Phys. Rev. Lett.* **108**, 264506.

THORODDSEN, S. 2002 The ejecta sheet generated by the impact of a drop. *J. Fluid Mech.* **451**, 373–381.

THORODDSEN, S., THORAVAL, M.-J., TAKEHARA, K. & ETOH, T. 2012 Micro-bubble morphologies following drop impacts onto a pool surface. *J. Fluid Mech.* **708**, 469–479.

THORODDSEN, S. T., ETOH, T. G. & TAKEHARA, K. 2003 Air entrapment under an impacting drop. *J. Fluid Mech.* **478**, 125–134.

THORODDSEN, S. T., ETOH, T. G., TAKEHARA, K., OOTSUKA, N. & HATSUKI, A. 2005 The air bubble entrapped under a drop impacting on a solid surface. *J. Fluid Mech.* **545**, 203–212.

TRAN, T., DE MALEPRADE, H., SUN, C. & LOHSE, D. 2013 Air entrainment during impact of droplets on liquid surfaces. *J. Fluid Mech.* **726**, R3.

TRYGGVASON, G., SCARDOVELLI, R. & ZALESKI, S. 2011 *Direct Numerical Simulations of Gas-Liquid Multiphase Flows*. Cambridge University Press.

WAGNER, H. 1932 Über Stoss und Gleitvorgänge und der Oberfläshe von Flüssigkeiten. *Z. Angew. Math. Mech.* **12** (4), 193–215.

WANG, A.-B., KUAN, C. C. & TSAI, P.-H. 2013 Do we understand the bubble formation by a single drop impacting upon liquid surface? *Phys. Fluids* **25**, 101702.

WILSON, S. & DUFFY, B. 1998 On lubrication with comparable viscous and inertia forces. *Q. J. Mech. Appl. Maths* **51**, 105–124.

XU, L., ZHANG, W. & NAGEL, S. 2005 Drop splashing on a dry smooth surface. *Phys. Rev. Lett.* **94**, 184505.

YARIN, A. & WEISS, D. 1995 Impact of drops on solid surfaces: self-similar capillary waves, and splashing as a new type of kinematic discontinuity. *J. Fluid Mech.* **283**, 141–173.

YARIN, A. L. 2006 Drop impact dynamics: splashing, spreading, receding, bouncing. *Annu. Rev. Fluid Mech.* **38**, 159–192.